

# Signatures of UV radiation around low-mass protostars in Serpens with IRAM 30 m

Agnieszka Mirocha<sup>1,2</sup>, Agata Karska<sup>2\*</sup>, Marcin Gronowski<sup>3</sup>, Lars E. Kristensen<sup>4</sup>, Miguel Figueira<sup>5</sup>, Marcin Gładkowski<sup>2,6</sup>, Łukasz Tychoniec<sup>7</sup>, Michał Żółtowski<sup>8</sup>

<sup>1</sup> Astronomical Observatory of the Jagiellonian University, ul. Orla 171, 30-244 Kraków, Poland

<sup>2</sup> Institute of Astronomy, Faculty of Physics, Astronomy and Informatics, Nicolaus Copernicus University, ul. Grudziądzka 5, 87-100 Toruń, Poland

<sup>3</sup> Institute of Physical Chemistry Polish Academy of Sciences, ul. Kasprzaka 44/52, 01-224 Warszawa, Poland

<sup>4</sup> Centre for Star and Planet Formation, Niels Bohr Institute and Natural History Museum of Denmark, University of Copenhagen, Øster Voldgade 5-7, DK-1350 Copenhagen K, Denmark

<sup>5</sup> National Centre for Nuclear Research, ul. Pasteura 7, 02-093 Warszawa, Poland

<sup>6</sup> Nicolaus Copernicus Astronomical Center, ul. Rabiańska 8, 87-100 Toruń, Poland

<sup>7</sup> Leiden Observatory, Leiden University, P.O. Box 9513, NL-2300RA Leiden, The Netherlands

<sup>8</sup> University of Le Havre, Laboratoire Ondes et Milieux Complexes, UMR CNRS 6294, 75 Rue Bellot, 76600 Le Havre, France

Received [Month] [Day], 2020; accepted [Month] [Day], 2020

## ABSTRACT

**Context.** Ultraviolet radiation (UV) influences the physics and chemistry of star forming regions, but its properties and significance in low-mass protostars are still poorly-understood.

**Aims.** We aim to identify and characterise the UV radiation in the surroundings of low-mass protostars on  $\sim 0.6 \times 0.6$  pc scales using the ratio of CN and HCN previously used for high-mass protostars. We focus on comparisons between protostar and outflow positions in the Serpens star-forming region and the validation of the proposed UV tracer for the corresponding physical conditions.

**Methods.** We present the  $5' \times 5'$  maps of Serpens encompassing 10 protostars with EMIR on IRAM 30 m in CN 1-0, HCN 1-0, CS 3-2, and their isotopologues. Radiative-transfer code RADEX and the chemical model Nahoon are used to determine column densities of molecules, gas temperature and density, and the UV field strength,  $G_0$ .

**Results.** Spatial distribution of HCN and CS emission resembles the CO 6-5 from APEX tracing outflows. CN emission is spatially associated with the positions of protostars, yet also extends to their immediate surroundings. Detection of the line wings in CN profiles suggest that at least some emission is produced in the outflows, likely as a product of HCN photodissociation. The ratio of CN and HCN total column densities is in the range from 1 to 10 corresponding to  $G_0$  of  $10^{-3} - 10^{-2}$ , for gas densities and temperatures typical for outflows of low-mass protostars.

**Conclusions.** UV radiation is identified towards both protostar and outflow positions, yet its strength is a factor of 10 lower than determined using OH and H<sub>2</sub>O ratios (Karska et al. 2018, ApJS). From the chemical viewpoint, the CN and HCN ratio is a more suitable tracer for UV fields characteristic for more massive protostars.

**Key words.** astrochemistry – stars: formation – ISM: molecules – ISM: individual objects: Serpens Main – Submillimeter: ISM

## 1. Introduction

Formation of low mass stars - the most numerous stellar population in galaxies (Kroupa 2002) - is associated with many physical phenomena. The inside-out collapse of dense envelopes is accompanied by the ejection of bipolar outflows and the formation of embedded disks (Frank et al. 2014; Harsono et al. 2015). UV radiation can be produced in accretion or bow shocks and irradiate the outflow cavities in the envelopes Spaans et al. 1995; van Kempen et al. 2009. The physical conditions and chemical composition in star forming regions strictly depend on the characteristics of the above processes.

The importance of UV radiation for star formation was initially considered only in the context of the formation of massive stars, where central stars are the main source of UV photons from early stages (Cesaroni 2005; Zinnecker & Yorke 2007).

Detail physico-chemical models of the envelopes and outflows with radiative transfer in 1 and 2D have been developed for high-mass protostars (Doty & Neufeld 1997; Stäuber et al. 2005; Bruderer et al. 2009). The far-UV radiation with photon energies  $< 13.6$  eV dissociates and ionizes molecules and atoms with ionization potentials below 13.6 eV; more energetic photons are easily absorbed in the surrounding interstellar medium (Gerin et al. 2016). Among the most useful diagnostics of the UV field in dense envelopes are abundances of hydrides and the column density ratio of CN and HCN (Stäuber et al. 2007). The corresponding UV field strengths are enhanced by at least 1-2 orders of magnitude compared to the interstellar radiation field and impact gas at temperatures of few hundred K (Stäuber et al. 2007; Benz et al. 2016).

In low-mass protostars, the possible role of UV radiation was realised due to detection of narrow  $^{12}\text{CO } J = 6 - 5$  lines spatially associated with outflow cavities in HH 46 van Kempen et al. (2009). Firm detection of [C I] 2-1 at the tip of the HH46 jet

\* Corresponding author: Agata Karska  
e-mail: agata.karska@umk.pl

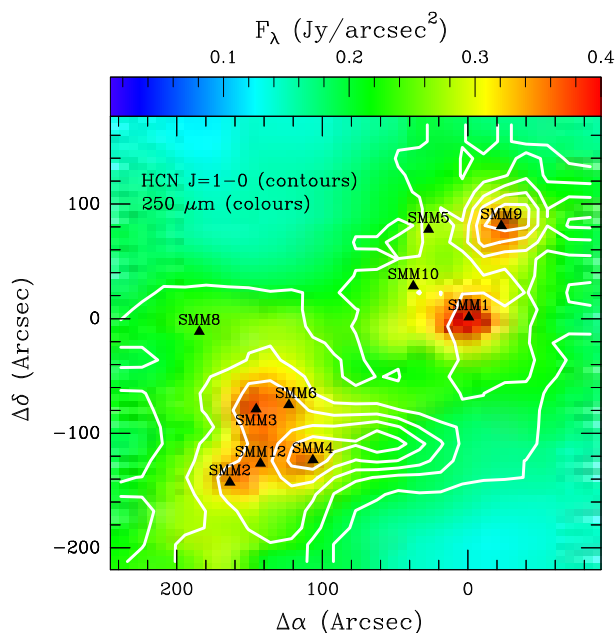


Fig. 1: EMIR map of HCN 1-0 (contours) on top of the continuum emission at  $250\ \mu\text{m}$  with *Herschel*/SPIRE. The HCN contours start at  $0.4\ \text{K km s}^{-1}$  and are drawn in steps of  $4\ \text{K km s}^{-1}$ . Information about the protostars is shown in Table 1.

and the lack of CO was attributed to the presence of dissociative bow shock capable of producing extra UV photons (Neufeld & Dalgarno 1989). Their transport on  $\sim 1000\ \text{AU}$  scales is facilitated by the low densities and scattering in the outflow cavities (Spaans et al. 1995). Similar signatures of UV radiation were seen in a dedicated APEX CHAMP<sup>+</sup> survey of  $\sim 20$  protostars (Yildiz et al. 2012, 2015).

Far-infrared observations with *Herschel* provided access to CO lines with  $J_u$  up to 49, and resulted in the detection of new hydrides, e.g.  $\text{OH}^+$  (Wyrowski et al. 2010) and  $\text{H}_2\text{O}^+$  (Ossenkopf et al. 2010). As part of the ‘Water in star-forming regions with *Herschel*’ (WISH, van Dishoeck et al. 2011a) key program, a statistically significant sample of low-mass protostars was surveyed with the Heterodyne Instrument for the Far-Infrared (HIFI, de Graauw et al. 2010) and the Photodetector Array Camera and Spectrometer (PACS, Poglitsch et al. 2010). Among the key findings are: (i) ubiquitous gas at temperature of  $\sim 300\ \text{K}$  with molecular signatures resembling shocks (Herczeg et al. 2012; Goicoechea et al. 2012; Karska et al. 2013); (ii) a consistently low abundance of  $\text{H}_2\text{O}$  of  $\sim 10^{-6}$  (Kristensen et al. 2017); (iii) high abundances of the products of  $\text{H}_2\text{O}$  photodissociation and other hydrides, in particular OH (Wampfler et al. 2013; Benz et al. 2016); (iv) velocity-resolved components in  $\text{H}_2\text{O}$  profiles arising close to the protostar, at the positions of hydrides (Kristensen et al. 2013); (v) ratios of  $\text{H}_2\text{O}/\text{OH}$  and  $\text{CO}/\text{OH}$  consistent with UV-irradiated shock models (Karska et al. 2018). All these pieces of evidence confirm the presence of UV photons in the immediate surroundings of low-mass stars.

In this paper, we analyze large-scale maps in HCN and CN as alternative tracers of UV photodissociation in low-mass star forming region in Serpens to address the following questions: What is the morphology and spatial extent of the regions affected by UV radiation? Are there systematic differences in the ratios of CN and HCN between protostar and outflow positions? Does chemical models validate the utility of this ratio as a tracer of

UV-irradiated gas in regions forming low-mass stars? What is the typical strength of UV radiation in Serpens determined from CN and HCN, and how it compares to the results from *Herschel*?

The paper is organized as follows. §2 describes the studied region and its protostars, the observations and data reduction. §3 show the submillimeter maps and the line profiles at selected positions. §4 shows the determination of molecular column densities and their comparisons to the Nahoon chemical model. §5 discusses the results in the context of complementary studies and §6 presents the summary and conclusions.

## 2. Source sample and observations

### 2.1. Serpens as a low-mass star-formation site

The Serpens star forming region is a well-studied, low-mass site of star formation at the distance of  $436 \pm 9\ \text{pc}$  (Ortiz-León et al. 2017). The identification and classification of young stellar objects in the region was done as part of the *Spitzer* ‘From Molecular Cores to Planet-forming Disks’ (c2d) survey (Harvey et al. 2007; Enoch et al. 2009; Evans et al. 2009; Dunham et al. 2015). Submillimetre sources were studied by continuum observations at 12, 25, 60, 100  $\mu\text{m}$  (Hurt & Barsony 1996), 800, 1100, 1300 and 2000  $\mu\text{m}$  (Casali et al. 1993) and 3 mm (Testi & Sargent 1998). The outflow activity in the cloud core was characterized using CO 2-1 (Davis et al. 1999), and more recently CO 3-2 and CO 6-5 for a subsample of sources (Dionatos et al. 2010, Yıldız et al. 2015). Ser SMM1, SMM3 and SMM4 were observed with *Herschel* as part of the WISH and ‘Dust, Ice, and Gas in Time’ (DIGIT, Green et al. 2013, 2016; Yang et al. 2018) programs.

Figure 1 shows the continuum map at  $250\ \mu\text{m}$  corresponding to the region that we observed with IRAM 30 m. The map was obtained with the *Herschel* Spectral and Photometric Imaging Receiver (SPIRE; Griffin et al. 2010) as part of the ‘*Herschel* Gould Belt survey project’ (André et al. 2010).

For the purpose of our analysis, we re-calculated spectral energy distributions (SEDs) for all protostars in the region using the continuum measurements at 70, 160, 250, 350 and 500  $\mu\text{m}$  from PACS and SPIRE covering the peak of the SEDs and following the procedures outlined in (André et al. 2010), (Dionatos et al. 2010), (Yildiz et al. 2015). Appendix A shows the final spectral energy distributions and provides the table with flux densities at each wavelength. Table 1 shows bolometric luminosities and temperatures, and the classification of the sources as Class 0 and I based on the later (Evans et al. 2009).

### 2.2. Observations and data reduction

The observations with IRAM 30 m were performed between 14 and 17 July 2009 as part of the project ‘HCN/CN as UV-tracers in YSO envelope-outflow interfaces’ (PI: L. Kristensen). The Eight Mixer Receiver (EMIR) bands E090 and E150 covering 73-117 GHz and 125-184 GHz were used targeting HCN 1-0 and CN 1-0, respectively. The broad frequency ranges of EMIR facilitated additional detections of  $\text{C}^{34}\text{S}\ 3-2$ ,  $\text{H}^{13}\text{CN}\ 1-0$  and  $\text{H}^{13}\text{CN}\ 2-1$ . The backend was the Versatile Spectrometer Array (VESPA) autocorrelator and the 1 MHz filterbank reaching the spectral resolution of 39 kHz (E150 band) and 78 kHz (E090 band). Table 2 shows the full list of transitions observed with EMIR with respective beam sizes and the main beam efficiencies used to convert antenna temperatures to the main beam temperatures.

Table 1: Luminosities and bolometric temperatures of targeted protostars in Serpens

Source	R.A. (J2000.0)	Decl. (J2000.0)	$T_{\text{bol}}$ (K)	$L_{\text{bol}}$ ( $L_{\odot}$ )	Class	Other names
SMM 1	18 29 50.0	+01 15 20.3	35	78.7	0	Ser-emb6, FIRS1, EC41, Bolo23
SMM 2	18 30 00.5	+01 12 57.8	31	4.1	0	Ser-emb4, Bolo28
SMM 3	18 29 59.6	+01 13 59.2	35	6.9	0	Ser-emb26, Bolo26
SMM 4	18 29 57.0	+01 13 11.3	77	4.4	I	Ser-emb22, Bolo25
SMM 5	18 29 51.4	+01 16 38.3	151	3.7	I	Ser-emb21, EC53, WMW24, Bolo22
SMM 6	18 29 57.8	+01 14 05.3	532	43.1	I	Ser-emb30, EC90, WMW35, SVS20S, Bolo 28
SMM 8	18 30 01.9	+01 15 09.2	15	0.2	0	Bolo30
SMM 9	18 29 48.3	+01 16 42.7	35	10.3	0	Ser-emb8, ISO241, WMW23, Bolo22
SMM 10	18 29 52.3	+01 15 48.8	83	6.2	I	Ser-emb12, WMW21, Bolo 23
SMM 12	18 29 59.1	+01 13 14.3	97	5.7	I	Ser-emb19, Bolo28

Source coordinates are adopted from Suresh et al. 2016 except of Ser SMM8, which position is listed in Lee et al. 2014).

Table 2: Catalog of the observed molecular lines with IRAM and APEX

Mol.	Trans.	$E_u/k_B$ (K)	Freq. (GHz)	Telescope	Beam size ( $''$ )	Efficiency $\eta_{\text{MB}}$
HCN	1-0	4.25	88.631847	IRAM-EMIR	28	0.81
H <sup>13</sup> CN	1-0	4.14	86.340184	IRAM-EMIR	29	0.81
	2-1	12.43	172.677881	IRAM-EMIR	14	0.68
CN	1-0	5.45	113.490985	IRAM-EMIR	22	0.78
C <sup>34</sup> S	3-2	13.9	144.617109	IRAM-EMIR	16	0.74
CS	3-2	14.1	146.969029	IRAM-EMIR	16	0.74
<sup>12</sup> CO	6-5	116.2	691.473076	APEX-CHAMP+	9	0.48

Molecular data adopted from the Leiden Atomic and Molecular Database (LAMDA, Schöier et al. 2005) and the JPL database (Pickett et al. 1998).

The OTF mode was used to obtain two maps with the sizes of  $300'' \times 300''$  and map centers at  $(\alpha_{\text{J2000}}, \delta_{\text{J2000}}) = 18^{\text{h}}29^{\text{m}}49.6^{\text{s}}, +01^{\circ}15'20.5''$ , and  $18^{\text{h}}29^{\text{m}}56.6^{\text{s}}, +01^{\circ}14'00.3''$ . Figure 2 shows the size and extent of the maps after the merging procedure and beam convolution. The merging and data reduction was carried out with the CLASS package within GILDAS<sup>1</sup>. For the sake of analysis, the EMIR spectra were baseline-corrected and resampled to a resolution of 0.5 km/s. The rms of extracted spectra varies from 0.024 K to 0.125 K.

The CHAMP+ dual-beam heterodyne receiver on the Atacama Pathfinder Experiment (APEX) telescope used for CO 6-5 observations at 691.5 GHz originally presented in Yıldız et al. 2015. The observations were performed on 16 June 2009 using position-switching in on-the-fly mapping mode resulting in maps covering  $340'' \times 340''$ . The Fast Fourier Transform Spectrometer (FFTS) was used as the backend with a resolution of  $0.079 \text{ km s}^{-1}$  (Klein et al. 2006). Typical value of rms is  $\approx 0.018$  K. Similarly, observations of the Ser SMM1 protostar in C<sup>18</sup>O were obtained with the APEX/CHAMP+ on 23 October 2009. The data reduction and analysis was performed in a similar fashion to the IRAM observations using the CLASS software.

### 3. Results

In the following sections, we present IRAM 30 m maps and line profiles providing complementary information about the emission from protostars and their outflows, and large-scale cloud emission. Differences in spatial extent reflect the range of gas

and dust distribution and associated physical conditions and processes. We calculate ratios of various transitions to pin-point species tracing similar physical components, the gas temperature, and line opacities.

#### 3.1. Spatial extent of line emission

Figure 2 shows the line emission associated with protostars and their outflows in Serpens obtained in HCN, CN, CS lines with EMIR on IRAM 30 m and CO with CHAMP+ on APEX. The emission in HCN and CN is the sum of all hyperfine components detected in the spectra (see Figure 3.2). Maps in additional transitions are presented in Appendix B.

HCN 1-0 emission, similar to other species, is associated with clusters of protostars in the SE and NW parts of the map where dust emission at  $250 \mu\text{m}$  is also detected (Figure 1). The emission peaks are the strongest at the positions of Ser SMM4 and SMM9 protostars and their outflows, and significantly weaker at Ser SMM1 and SMM3. Qualitatively, the pattern of emission in HCN is similar to the CO 6-5 - the well-established outflow tracer (Figure 2; bottom right panel). This results is in agreement with previous surveys of HCN in low-mass protostars (Bachiller et al. 2001; Walker-Smith et al. 2014). Any differences between HCN and CO likely stem from the higher critical density of the HCN 1-0 ( $\sim 10^6 \text{ cm}^{-2}$ ), its lower upper energy level (see Table 2), and its significantly easier photodissociation due to UV photons than CO (see §5).

CS 3-2 emission shows a very similar spatial distribution to HCN 1-0 and CO 6-5, with most prominent structures associ-

<sup>1</sup> See <http://www.iram.fr/IRAMFR/GILDAS>

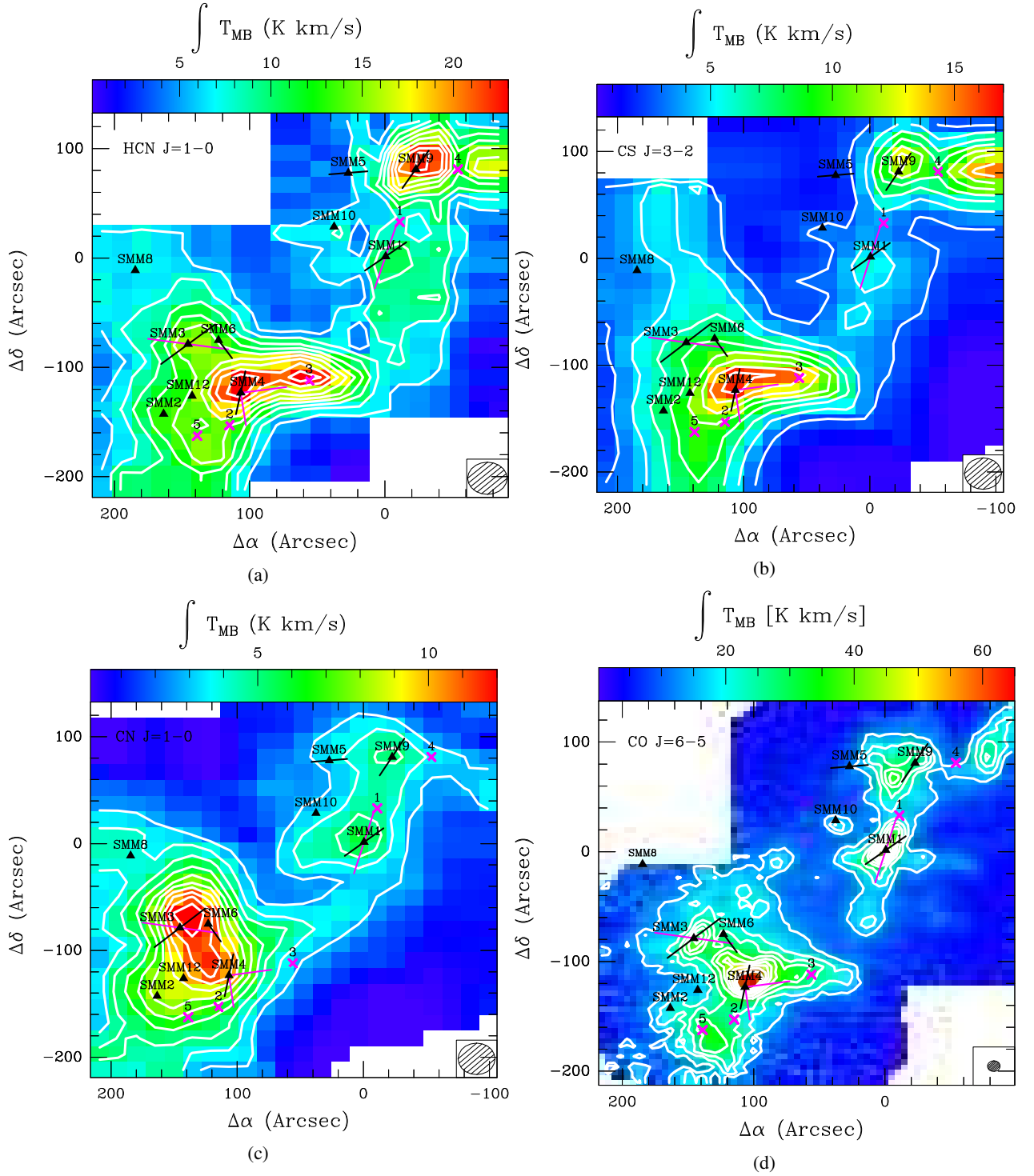


Fig. 2: Integrated intensity maps of the HCN 1-0 (upper left panel), CS 3-2 (upper right panel), CN 1-0 (bottom left panel) and CO 6-5 (bottom right panel) in Serpens star-forming region with IRAM 30 m. Black triangles show the positions of protostars (see Table 1) and magenta crosses show the outflow positions selected for analysis (see Table 3). Solid lines show outflow directions from CO 6-5 (black; Yıldız et al. 2015) and CO 3-2 (magenta; Dionatos et al. 2010). The center of the maps (0,0) corresponds to (RA, DEC)= 18<sup>h</sup>29<sup>m</sup>46.6<sup>s</sup>, 01°18'20.5". Contour levels start at 30  $\sigma$  for HCN and CN and increase every 10  $\sigma$ . For CS and CO, the first contours are at 10  $\sigma$  and 70  $\sigma$  levels, and the steps are 5  $\sigma$  and 30  $\sigma$ , respectively.

ated with Ser SMM4. Some differences are seen mostly in the surrounding of Ser SMM9, where CS emission is substantially weaker at the Ser SMM9 position than in Ser SMM4, in contrast to HCN which shows similar line strengths towards both protostars. Additionally, CS shows a relatively strong emission to the

W of Ser SMM9, which coincides with the outflow from S68N - with the protostar itself located outside of the map (Kristensen et al. 2010). The differences may result from CS tracing warmer, yet lower-density gas ( $n_{\text{crit}} \sim 10^5 \text{ cm}^{-3}$ ).

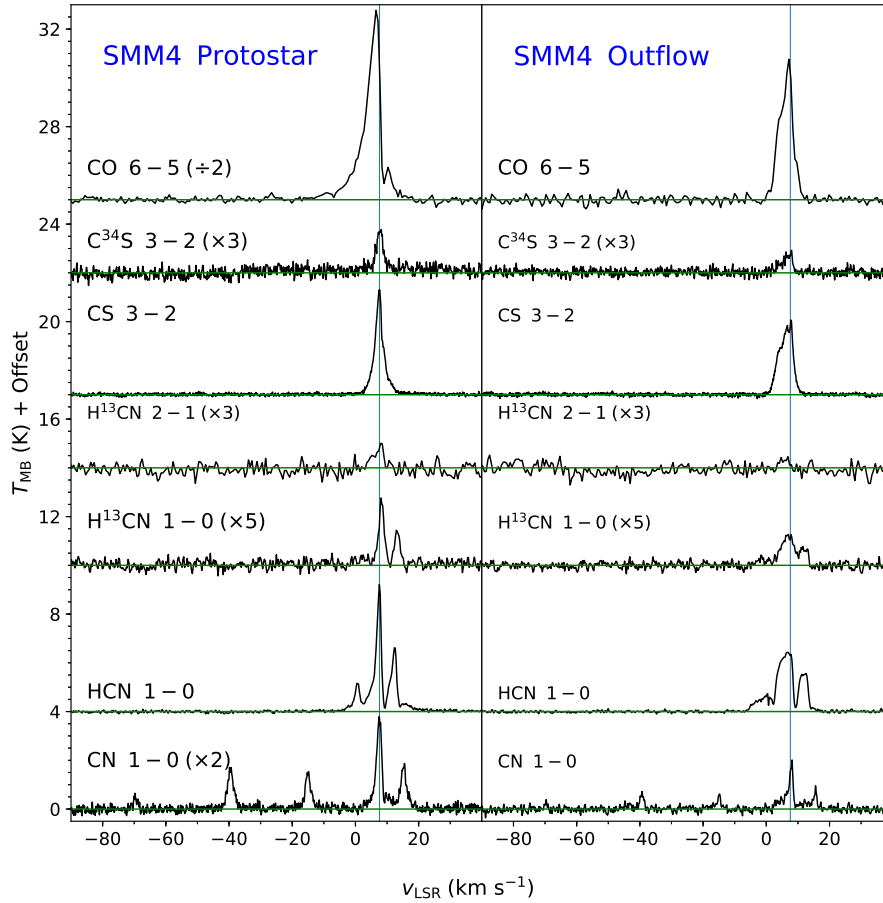


Fig. 3: Line profiles of CO 6-5,  $C^{34}S$  3-2, CS  $J = 3 - 2$ ,  $H^{13}CN$  1-0, HCN 1-0 and CN 1-0 lines at the protostar position Ser SMM4 (left) and the associated outflow position nr 3, see Table 3 (right). Spectra of CO 6-5,  $C^{34}S$  3-2,  $H^{13}CN$  and CN are scaled in flux by a factor of 0.5, 3, 5 and 2, respectively. The  $H^{13}CN$   $J = 2 - 1$  line is not detected in the outflow position.

In contrast to HCN and CS, CN 1-0 emission is associated more closely with the positions of protostars and the continuum peaks at  $250\ \mu m$ , and not the outflows (Figures 1 and 2). The emission is the strongest at Ser SMM4, SMM3, and SMM6, and the region in between these three protostars. The differences in spatial extent between CN and the outflow tracers suggest a different physical origin (see §5).

### 3.2. Detection rates and line profiles

To explore gas properties in Serpens, we selected 10 protostar positions and 5 outflow positions for more in-depth analysis (see Tables 1 and 2, and Figure 2). Figure shows line profiles of targeted species and transitions toward Ser SMM4 and its outflow. Appendix C shows the line profiles at each selected position and the table with line fluxes.

All targeted species and their isotopologues were detected in each and every position of the protostars in Serpens, except the  $H^{13}CN$  2-1 which was detected only in Ser SMM4 and Ser SMM9. Similarly, emission in the outflow positions was always detected in HCN, CS, CN and CO. Detections in the targeted lines isotopologues were seen in  $C^{34}S$  3-2,  $H^{13}CN$  1-0, but not in  $H^{13}CN$  2-1. In case of HCN and CN, up to 3 and 5 components are detected as the result of the hyperfine splitting, respectively.

The line shapes at both protostar and outflow positions show a relatively broad profiles, with outflow wings in CS extending

of  $13.6\ km\ s^{-1}$  and  $9.8\ km\ s^{-1}$  at Ser SMM4 source and outflow, respectively (Figure 3.2). Clearly, the beam sizes of IRAM encompass a substantial amount of outflow emission even at the protostar position.

In order to quantify the emission in the line wings, we use the line profile of  $C^{18}O$  6-5 for Ser SMM1, which is a good envelope tracer. The profile extends from  $7.8\ km\ s^{-1}$  to  $9.4\ km\ s^{-1}$  - the velocity ranges we exclude for the intensity integration of our line profiles. The outer velocity ranges for each of the profiles are calculated for each line separately based on the measured rms and the  $2\ \sigma$  signal. Appendix D shows the table with calculated intensities in the line wings for all selected positions.

In case of Ser SMM4 (Figure 3.2), the emission in the line wings of CS 3-2 is 61% of the total profile in the protostar position and 72% in the outflow position. Similar characteristics is seen in HCN line wings (48% and 68%, respectively). In contrast, CN 1-0 is detected mostly at source velocity, with only 40% of emission in the line wings. Among all 15 positions, exceptionally broad line wings in HCN and CS are detected in the Ser SMM1, Ser SMM9 and Ser SMM10 protostar positions and outflow positions nr 1, 4, and 5 (Table 3), exceeding 70% of the total profile in HCN and 58% in CS.

The shapes of line profiles clearly indicate that the emission in various species is detected in different physical components of the protostellar systems. For the sake of our forthcoming analysis, we will consider the emission in the line wings alone and in the fully integrated profiles separately.

Table 3: Molecular line ratios of the fully integrated line profile and the line wings

Source	CN / HCN		CS / CO		HCN / CO		HCN / H <sup>13</sup> CN		CS / C <sup>34</sup> S	H <sup>13</sup> CN 2-1/1-0
	Full	Line wings	Full	Line wings	Full	Line wings	Full	Line wings	Full	Full
Protostar positions										
Ser SMM1	0.61	0.40	0.08	0.05	0.14	0.10	6.51	12.45	4.66	-
Ser SMM2	0.65	0.53	0.38	0.23	0.58	0.35	8.74	22.28	9.98	-
Ser SMM3	0.85	0.57	0.16	0.10	0.27	0.10	25.99	42.90	16.50	-
Ser SMM4	0.47	0.40	0.16	0.12	0.23	0.13	13.43	14.91	9.88	1.98
Ser SMM5	0.67	0.31	0.19	0.09	0.31	0.17	5.26	-	7.95	-
Ser SMM6	0.81	0.55	0.29	0.19	0.44	0.14	15.10	17.39	11.19	-
Ser SMM8	0.43	0.27	-	-	-	-	49.39	117.19	17.57	-
Ser SMM9	0.24	0.11	0.34	0.30	0.57	0.49	8.73	16.33	6.78	1.31
Ser SMM10	0.41	0.15	0.14	0.09	0.29	0.23	7.00	31.11	9.12	-
Ser SMM12	0.71	0.63	0.57	0.40	0.82	0.49	8.84	10.82	17.70	-
Outflow positions										
1 (-11.00,33.00)	0.58	0.24	0.24	0.15	0.43	0.31	9.87	-	4.16	-
2 (114.86,-153.00)	0.51	0.47	0.35	0.24	0.47	0.27	13.48	27.12	10.71	-
3 (56.00,-112.00)	0.13	0.03	0.54	0.56	0.74	0.72	11.92	12.29	15.57	-
4 (-54.00,81.00)	0.25	0.13	0.63	0.54	0.97	0.84	8.38	12.12	8.90	-
5 (138.86,-162.60)	0.56	0.49	0.26	0.18	0.36	0.21	9.05	11.52	9.76	-

Sources in the upper part of the table refer to the positions of protostars within the IRAM maps (Figure 1 and 2), positions in the lower part refer to selected outflow positions on the same maps. Coordinates of the outflow positions refer to J2000 RA 18:29:49.6 and DEC 01:15:20.5.

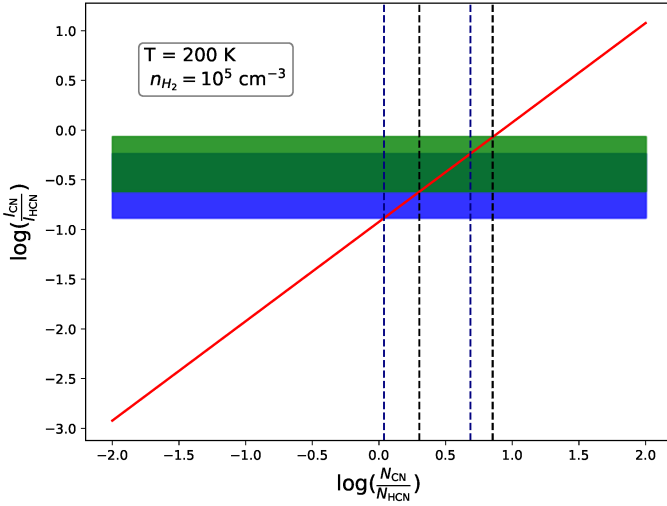


Fig. 4: The ratio of CN and HCN column densities obtained with RADEX for  $n_{\text{H}} = 10^5 \text{ cm}^{-3}$  and  $T_{\text{kin}} = 200 \text{ K}$  (red line). The observed line intensity ratio is shown as a rectangle, with green color corresponding to the values observed at the protostar position and blue color for the outflow positions. Column density ranges are marked with black and navy dashed lines for protostars and outflow positions, respectively.

### 3.3. Line ratios

Table 3 shows the molecular line ratios at protostar and outflow positions in Serpens calculated separately for the fully integrated profiles and for the line wings. Here, we will discuss the results for (i) ratios of different isotopologues, informing about the line opacities, (ii) the ratio of two transitions of H<sup>13</sup>CN, indicating gas temperature, (iii) ratios of different species, reflecting their relative abundances.

Table 4: Model-dependent column density ratios of CN and HCN

$n_{\text{H}_2}$ ( $\text{cm}^{-3}$ )	$T_{\text{kin}}$ (K)	$\log_{10}(\text{N}(\text{CN})/\text{N}(\text{HCN}))$ protostars	$\log_{10}(\text{N}(\text{CN})/\text{N}(\text{HCN}))$ outflows
$10^4$	30	0.24-0.79	-0.02-0.63
$10^4$	75	0.16-0.71	-0.10-0.55
$10^4$	200	0.12-0.67	-0.14-0.51
$10^5$	30	0.28-0.83	0.016-0.67
$10^5$	75	0.27-0.82	0.00-0.65
$10^5$	200	0.30-0.85	0.04-0.69
$10^6$	30	0.38-0.92	0.10-0.75
$10^6$	75	0.43-0.98	0.16-0.81
$10^6$	200	0.50-1.05	0.23-0.88

#### 3.3.1. Ratios of different isotopologues

The line ratio of the same transition of two isotopologues can be used a tracer of line opacity of the more abundant species, assuming that the emission in the other isotopologue is optically thin. We adopt a standard method described in (Goldsmith et al. 1984) to determine the line opacities of HCN 1-0 and CS 3-2 lines, both in the protostar and outflow positions. We assume that both isotopologues arise from the same physical region, described by the excitation temperature,  $T_{\text{exc}}$ , and in local thermodynamical equilibrium (LTE). Using the equation 1, we obtain the values of 0.3-5.7 and 0.3-4.8 for the fully-integrated line profiles of HCN and CS with their isotopologues respectively.

$$\frac{T_{\text{HCN}}}{T_{\text{H}^{13}\text{CN}}} = \frac{X[\text{HCN}]}{X[\text{H}^{13}\text{CN}]} \frac{1 - \exp(-\tau_{\text{HCN}})}{\tau_{\text{HCN}}} \quad (1)$$

For comparison, the expected ratio in case of optically emission is 30 and 20 for the HCN/H<sup>13</sup>CN (Daniel et al. 2013) and CS/C<sup>34</sup>S (Tercero et al. 2010) ratios, respectively. Thus, the emission in both species is optically thick, when the entire profile is considered. In contrast, the **HCN/H<sup>13</sup>CN ratio measured in the line wings is around 10-40 (except Ser-SMM8). It correspond to the optical depth of 0.6-2.6 that is comparable to**



the optically thin ratio. **Similarly, line ratio of CS/C<sup>34</sup>S can be translated to  $\tau \approx 0.8 - 2.6$ .** Thus, in the selected velocity ranges the ratios of line emission is these species are a valuable measure of real emission.

We note that an alternative method of calculating the line optical depths is to check the ratios of various components due to hyperfine splitting. However, for HCN show considerable anomalies (Loughnane et al. 2012). The method can be applied to CN molecular lines based on three the strongest components  $F=3/2 \rightarrow 1/2$ ,  $F=5/2 \rightarrow 3/2$ ,  $F=1/2 \rightarrow 1/2$  with ratio of 0.1235:0.3333:0.0988 (Skatrud et al. 1983). The optical depth varies from 0.4 to 1.6 and from 0.2 to 1.0 for protostars and outflows positions, respectively.

The calculated optical depths are in agreement with the calculations performed using the 1D radiative-transfer code RADEX (van der Tak et al. 2007). Assuming column density of HCN of  $3 \times 10^{14} \text{ cm}^{-2}$ , hydrogen density of  $10^5 \text{ cm}^{-3}$  and kinetic temperature of the gas of 50 K, the optical depths of HCN is 4.4. For CS, the value is 2.1, assuming column density of  $5 \times 10^{13} \text{ cm}^{-2}$ .

### 3.3.2. The H<sup>13</sup>CN 2-1/1-0 ratio

The H<sup>13</sup>CN 2-1 emission was detected in two positions only: Ser-SMM4 and Ser-SMM9. The ratio of two lowest transitions is 1.98 and 1.31 respectively. Based on two different transitions of the same molecule, the excitation temperature can be calculated using Equation 2, where  $E_i$  refers to energy and  $n_i$  refers to population of upper and lower level.

$$T_{\text{ex}} = \frac{E_u - E_l}{k \ln \frac{n_l}{n_u}} \quad (2)$$

The excitation temperature equals 2.43 K and 2.77 K for Ser-SMM4 and Ser-SMM9 respectively. These values are much lower than expected in the envelopes and outflows of low-mass protostars, and likely affected by the low signal-to-noise of the detected lines. **? found the excitation temperatures for Ser-SMM1, Ser-SMM3 and Ser-SMM4 using rotational diagrams. Based on <sup>13</sup>CO and C<sup>18</sup>O the excitation temperature of the envelope is about 40-60 K. The <sup>12</sup>CO emission in connected with the outflows with kinetic temperature of 70-100 K.**

### 3.3.3. Ratios of different species

The median value of the CN/HCN ratio at the protostars positions is  $0.63 \pm 0.19$ . Slightly lower ratio is calculated for the outflow positions and equals  $0.51 \pm 0.20$ . The CN and HCN ratio varies between 0.13 at the Outflow 3 to 0.85 at the Ser-SMM3.

There is no significant dependence between the CN and HCN ratio and the evolutionary stage of a source. The ratio for the Class 0 protostars is  $0.61 \pm 0.23$  and for the Class I protostars is  $0.67 \pm 0.17$ .

## 4. Analysis

In this section, we calculate column densities of the molecules with the aid of radiative-code RADEX and compare them to the results from the chemical-code Nahoon, run for a set of gas temperatures, densities and UV radiation fields.

### 4.1. Column densities of molecules from observations

In case of optically thin lines and the LTE conditions, the column density of the upper level of a given molecule,  $N_u$ , can be calculated using the equation 3. Here,  $\beta$  is a constant equal  $1937 \text{ cm}^{-2}$ ,  $W$  is the integrated intensity of the emission line ( $\int T_{mb} dV$ ), and  $\nu$  is a transition frequency in GHz.

In order to calculate the total column density of a given molecule, we adopt the gas temperature of 75 K (see §3.3.2). Equation 4 takes into account the temperature-dependent partition function  $Q(T)$  for a given molecule, and the upper level energies ( $E_u$ ) and level degeneracies ( $g_u$ );  $k$  is a Boltzmann constant. Appendix E shows the results obtained for all observed molecules, both for the fully-integrated line profiles and the lines wings.

$$N_u = \beta \frac{\nu W}{A} \quad (3)$$

$$N_{\text{tot}} = Q(T_{\text{exc}}) \exp\left(\frac{E_u}{k T_{\text{exc}}}\right) \frac{N_u}{g_u} \quad (4)$$

Because of the optical thickness of HCN (§3.3.1), we also employ the non-LTE radiative transfer code RADEX to obtain independent determinations of the column densities. In order to mimic the optically thin case, for the calculations we adopt the HCN column density of  $10^8 \text{ cm}^{-2}$ . We vary the column density of CN from  $10^6 \text{ cm}^{-2}$  to  $10^{10} \text{ cm}^{-2}$ . The typical physical conditions of the gas in low-mass star forming regions are: number densities,  $n_H$  of the order of  $10^4 - 10^6 \text{ cm}^{-3}$  and kinetic temperature  $T_{\text{kin}}$  of 30-200 K. Table 4 shows the ratios of the calculated column densities of CN and HCN for these different sets of parameters, and assuming a line width of  $1.0 \text{ km s}^{-1}$ , for protostars positions and outflows separately.

The models are a means to translate the observed line ratios of CN and HCN into column densities ratios. Figure 4 shows **an example** model calculated for **200K and  $10^5 \text{ cm}^{-3}$** . **Similar models can be found in Fig. E.1** for the densities and temperatures typical for outflows in low-mass protostars (van Kempen et al. 2009, Yıldız et al. 2015). The observed line intensity ratio (full profile) in logarithm is in the range from -0.62 to -0.07 and from -0.87 to -0.24 for protostars and outflow positions, respectively. The corresponding column density ratio is in the range 0.12 to 1.05 and -0.14 to 0.88. Similar models were calculated for other sets of temperatures and densities, and the determined scaling factors between the intensity and column density ratios show a very weak dependence on the adopted physical parameters. The resulting column density ratios of CN and HCN are in order of 1-10.

### 4.2. Theoretical column densities from Nahoon

The Nahoon chemical code is used to calculate theoretical column densities of molecules for a set of physical conditions and UV field strengths; it is a well-known **almost or del(purely gas-phase)** purely gas-phase chemical code for astronomical applications (Wakelam et al. 2012).

The Nahoon solver computes the chemical evolution in time including 489 species and 6992 gas-phase and gas-grain reactions based on rate coefficients from the Kinetic Database for Astrochemistry (KIDA) database<sup>2</sup>. The Nahoon code can model chemistry at a fixed temperature and density (0D modeling), as

<sup>2</sup> <http://kida.obs.u-bordeaux1.fr/>

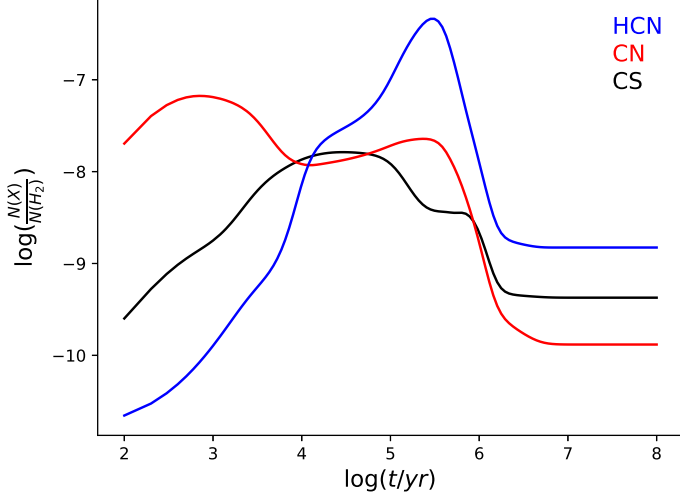


Fig. 5: Time evolution of CN (red line), HCN (blue line) and CS (black line) abundances obtained with Nohoon astrochemical code with initial parameters of  $n_H = 10^4 \text{ cm}^{-3}$ ,  $T = 10 \text{ K}$ ,  $A_V = 5 \text{ mag}$ . The assumed cosmic-ray ionization rate is  $1.3 \times 10^{17} \text{ s}^{-1}$ , dust to gas mass ratio is 0.01, dust grain radius is  $10^{-5} \text{ cm}$ , grain density is  $3 \text{ g cm}^{-3}$ .

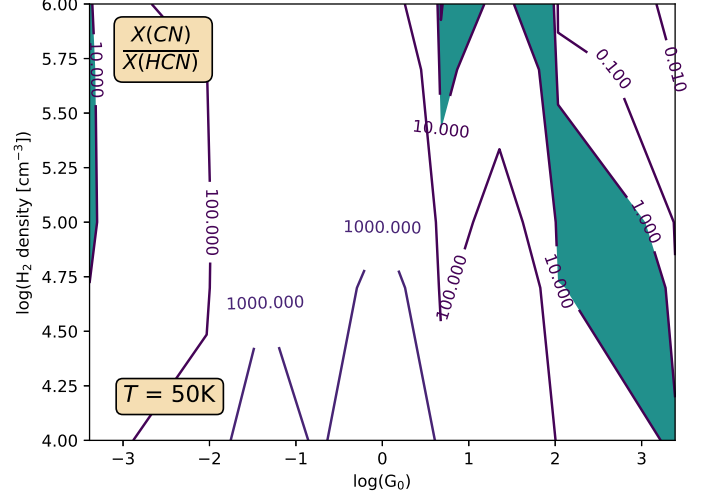


Fig. 7: The column ratio of CN and HCN from Nohoon for a range of hydrogen densities and UV field strengths assuming  $T$  equal 200 K (contours) and the observed column density ratios (in green).

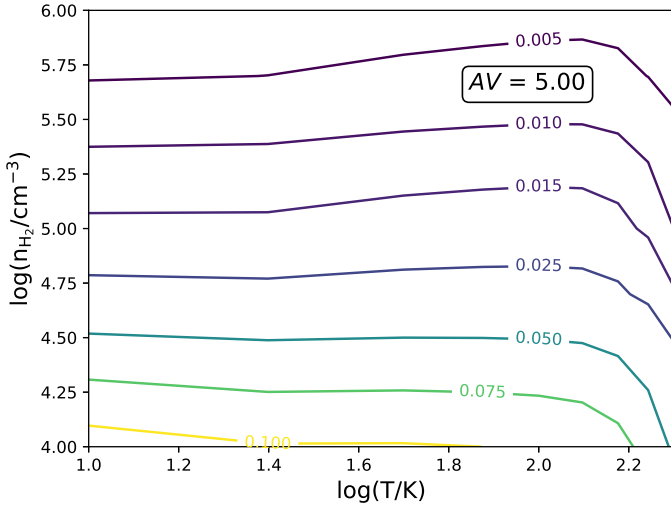


Fig. 6: Contour plot of Nohoon sets of models of CN/HCN abundances ratio with fixed visual extinction  $A_V = 5 \text{ mag}$  at the time of  $10^7 \text{ yrs}$  after star formation began in the cloud.

well as at grid of temperature, density and visual extinction (1D modeling).

The UV radiation in Nohoon is described through the relation between visual extinction  $A_V$  and the photodissociation rate coefficient  $k$  (equation 4). Here,  $\alpha$  and  $\gamma$  are coefficients of photodissociation of HCN equal to  $1.64 \times 10^{-9}$  and 3.12, respectively (Heays et al. 2017).

$$k = \alpha e^{-\gamma A_V} \quad (5)$$

In our analysis, we calculate 1D grid with the latest version of Nohoon code (Nohoon\_kida.uva.2014). The evolution of

the chemical network starts at the time of a dense cloud formation. Figure 5) shows a model corresponding to a typical dense cloud with temperature of 10 K and hydrogen total density of  $n_H = 10^4 \text{ cm}^{-3}$ . The chemical composition of the CN, HCN and CS molecules becomes stable at the time of  $10^7 \text{ yrs}$ ; the HCN abundance is higher than that of CN. We assume the time of  $10^6 \text{ yrs}$  as the moment when the star formation starts in a dense cloud. We use model abundances for all 489 species at this moment of time as an input data for the forthcoming set of models.

The closest neighbourhood of low-mass protostars is simulated based on the initial abundances of all species from starless cloud modelling. We adopt the cosmic-ray ionization rate of  $1.3 \times 10^{17} \text{ s}^{-1}$  (Cravens & Dalgarno 1978). The sets of models are run for the temperature range between 10 and 200 K and the total hydrogen densities from  $10^4 \text{ cm}^{-3}$  to  $10^6 \text{ cm}^{-3}$ .

Figure 6 show the model results assuming visual extinction of 5 mag **what corresponds to the lack of UV radiation**. In that case, HCN is more abundant than CN by about 2-3 orders of magnitude. The column density ratio of CN and HCN weakly depends on the gas temperature, **so we fix the gas temperature at 50K for envelopes of protostars and 200 K for outflows**.

In the next step, we run the model for the range of visual extinction between  $-2.5^m$  and  $2.5^m$  that corresponds to the UV radiation field  $G_0$  of  $4 \times 10^{-4}$  to  $2.4 \times 10^3$ . **The reaction network was corrected for HCNH<sup>+</sup> photodissociation. The HCNH<sup>+</sup> can be photodissociated into HCN<sup>+</sup> or HNC<sup>+</sup> molecules. We estimated the reaction rate coefficient as 10% of the HCN photodissociation rate. Figures 7 and 8 Show the ratio of CN and HCN abundances as a function of  $n_H$  and  $G_0$ . The observed ratios of 1-10 match the calculated ratios in three regimes: for very weak UV fields ( $< 10^{-3} G_0$ ), for the relatively weak UV fields of  $10^{-1} - 10^1$  and relatively strong UV fields of  $10^2 - 10^3$ .**



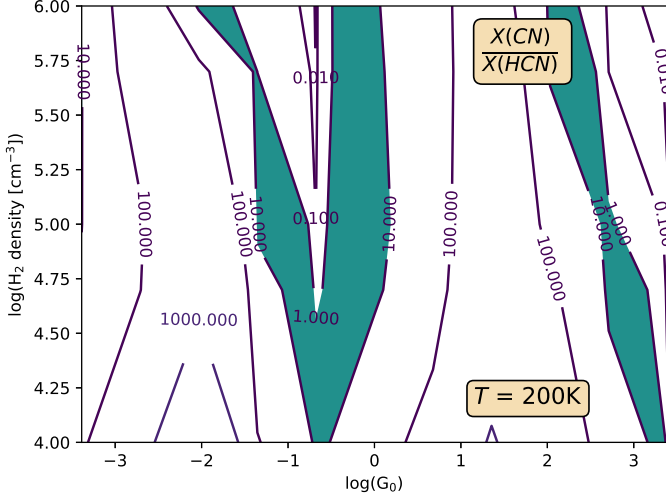


Fig. 8: Similar to Fig. 7 but for fixed temperature  $T = 50$  K.

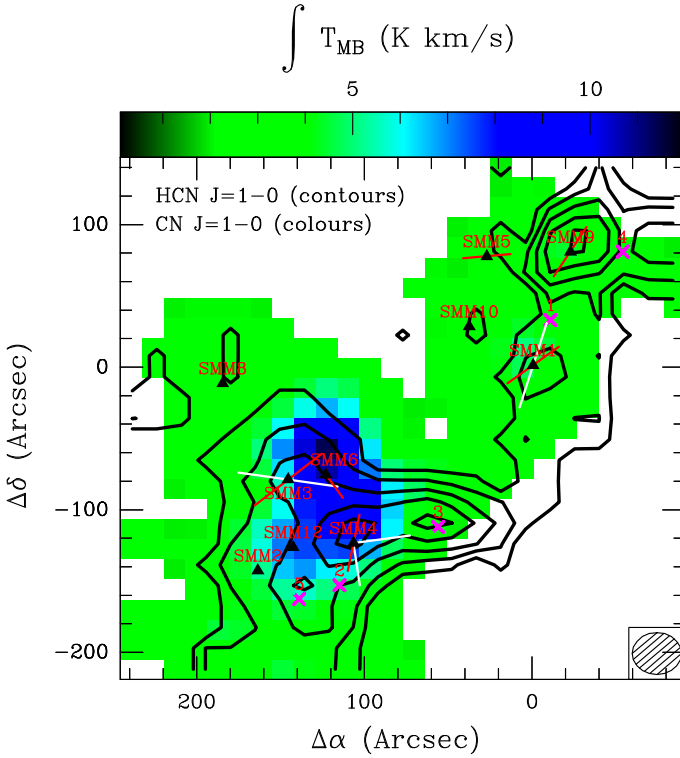


Fig. 9: Map of the intensity ratio of CN 1-0 (colours) and HCN 1-0 (contours) in Serpens. The labels are the same as in Figure 2. Contour levels start at  $30 \sigma$  with the steps of  $20 \sigma$ . The CN emission has been resampled to beam size of HCN in order to compare the same emitting regions.

## 5. Discussion

### 5.1. Comparison of the spatial extent of CN and HCN

The relative abundance of CN and HCN molecules is widely used as a tracer of UV radiation in different astronomical contexts: reflection nebulae (e.g. Fuente et al. 1995), proto-planetary disks (e.g. Chapillon et al. 2012), proto-brown dwarfs (e.g. Riaz et al. 2018). CN is a product of photodissociation of HCN with the

photodissociation rate of  $1.64 \times 10^{-9}$ . CN has smaller photodissociation rate of  $5.19 \times 10^{-10}$  (Heays et al. 2017), thus is not that sensitive for photodissociation as HCN. Since CN and HCN can be photodissociated selectively, therefore the CN/HCN ratio probes regions affected by UV emission. The ratio is the highest near the source of the UV emission, and decreases with the distance from the source (Fuente et al. 1993).

Figure 9 shows a large-scale map of CN 1-0 and HCN 1-0.

The CN  $J = 1 - 0$  transition is shifted to the north in respect to the HCN  $J = 1 - 0$  emission. It is highly concentrated in the SE subcluster, while the NW subcluster is dominated by the HCN. Both molecules show a diffusive ‘bridge’ between the two subclusters. It is connected with Ser-SMM4 and Ser-SMM1 outflows in HCN, while the CN follows the dust continuum emission. The emission in both molecules is anti-correlated north from Ser-SMM6 and west from Ser-SMM4 sources. At the dense area of Ser-SMM9 surrounding CN/HCN ratio is significantly weaker.

Both species have been detected in all sources positions. CN as a product of HCN photodissociation indicates other properties of low-mass protostars surroundings (Section 4). The highest CN/HCN integrated intensity ratio occurs in Ser-SMM6 and Ser-SMM3 protostars. On the other hand, Ser-SMM9 object is characterised by very low CN/HCN line ratio. Similarly low CN/HCN ratio is measured in outflow positions no. 3 and 4.

Most of the sources show high flux values in both molecules (Table 3). However, they present unequal levels which indicates regions of different properties. The CN/HCN ratio varies between protostars positions, as well as between off-source positions. **del? Repeated information: The highest CN/HCN ratio is found in Ser-SMM3, Ser-SMM6 and Ser-SMM12 sources.** This parameter seems to be not correlated with the evolutionary stage of a protostar. All the sources with the highest CN/HCN ratio are located in the SE subcluster. Ser-SMM3 and Ser-SMM6 are situated in close neighbourhood, in the area characterised by high emission of CN  $J = 1 - 0$  line. At Ser-SMM9 and Ser-SMM10 protostars the lowest CN/HCN ratio is observed. Both sources are young, Class 0 YSOs. In addition they are separated by  $\approx 45$  arcsec from the other sources.

**The same trend can be recognised in the integrated intensity ratio measure in the wings only. The highest ratio is present at the same protostars, although SMM12 shows the highest value in this case. It is located in 60 arcsec from the Ser-SMM3 and Ser-SMM6 protostars, in the area of with significantly lower level of HCN emission. No outflow is known from Ser-SMM12. The CO  $J = 6 - 5$  line in the neighbourhood of Ser-SMM12 does not indicate an outflow either. Extremely low CN and HCN ratio in the wings emission is connected with blue-shifted outflow from Ser-SMM4 (outflow position no. 3). In general the ratio is lower at outflow positions than at positions of protostars that indicates the UV radiation is produced in the closest neighbourhood of the protostars. The most prominent emission of the CN line is associated with the protostars concentration in the SE subcluster, rather than with the evolutionary stage of a source.**

### 5.2. UV field strengths in Serpens

Low CN/HCN ratio found in astrochemical model for strongly irradiated gas is a surprising result. Both production and destruction of each molecule need to be investigated in order to explain the reason behind HCN abundances being higher than expected. Detailed models of the most dominant reactions for destruction and production of each molecule are presented in Fig. F.1 –

Table 5: Dominant processes in CN and HCN chemistry at 50 K

Molecule	Weak UV fields ( $G_0 = 10^{-3} - 10^{-1}$ )	Medium UV fields ( $G_0 = 10^{-1} - 10^1$ )	Strong UV fields ( $G_0 = 10^1 - 10^6$ )
CN	$O + CN \rightarrow N + CO$ $CN + N \rightarrow C + N_2$	<b>Destruction</b> $CN + ph \rightarrow C + N$ $O + CN \rightarrow N + CO$	$CN + ph \rightarrow C + N$
	<b>Production</b> $N + CH \rightarrow H + CN$ $CNC^+ + e^- \rightarrow C + CN$ $N + C_2 \rightarrow C + CN$	<b>Production</b> $N + C_2 \rightarrow C + CN$ $H + CN^+ \rightarrow CN + H^+$	$HCN^+ + e^- \rightarrow H + CN$ $N + CH \rightarrow H + CN$ $H + CN^+ \rightarrow CN + H^+$ $N + C_2 \rightarrow C + CN$
		<b>Destruction</b> $HCN + C^+ \rightarrow H + CNC^+$ $HCN + ph \rightarrow H + CN$	$HCN + ph \rightarrow H + CN$ $HCN + C^+ \rightarrow H + CNC^+$
HCN	$HCN + C^+ \rightarrow H + CNC^+$ $HCN^+ + HCO^+ \rightarrow CO + HCNH^+$ $HCN + H^+ \rightarrow H + HNC^+$ $HCN + ph \rightarrow H + CN$	<b>Production</b> $H + CCN \rightarrow C + HCN$ $HCNH^+ + e^- \rightarrow H + HCN$	$HCNH^+ + e^- \rightarrow H + HCN$ $H + CCN \rightarrow C + HCN$
	$N + CH_2 \rightarrow H + HCN$ $H + CCN \rightarrow C + HCN$ $HCNH^+ + e^- \rightarrow H + HCN$ $C + HNC \rightarrow C + HCN$		

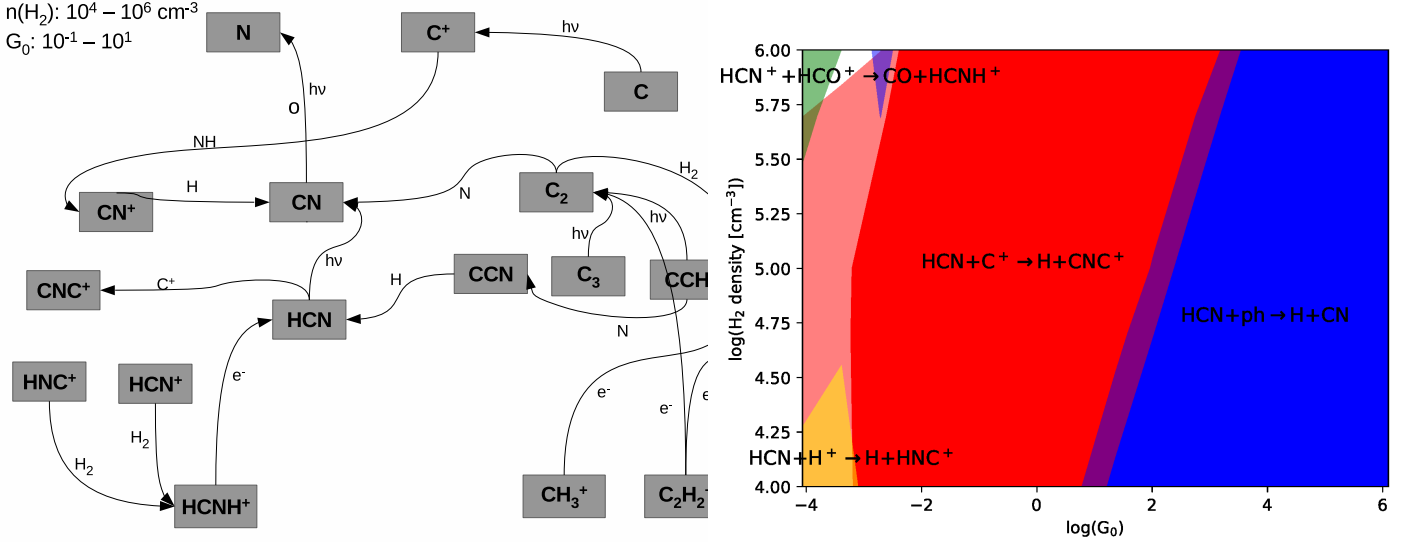
Fig. 10: Reactions network for UV irradiated gas of  $G_0 = 10^{-1} - 10^1$ .

Fig. F.2 with the assumption of fixed 50 K temperature. Reaction flux is defined as reactants abundances multiplied by reaction rate coefficient. Only these reactions were taken into consideration which accumulated flux is greater than 80% of the total flux of all reactions contributed in the studied molecules destruction or production.

The reactions distribution in the parameter space is not very strongly depended on hydrogen densities. The strength of an additional UV radiation source is the parameter that distinguishes the dominant reactions the most. It was divided into three regimes: with weak, intermediate and strong UV field. The reactions where CN or HCN production or destruction is greater than 30% are listed in Tab. 5 as well as illustrated in Fig. 10, as well as in Fig. F.4- Fig. F.5.

Fig. 11: Dominant reactions of HCN destruction. Reactions contributed at least 50% of total flux are marked with full colours. Transparent colours correspond to 30%-50% contribution.

In the regime of weak UV radiation fields dominant formation channels of CN and HCN are hydrocarbons (CH and  $CH_2$  respectively) reactions with atomic nitrogen. In more dense areas electron reaction with CNC cation plays role in the CN formation. The destruction of CN is mostly dominated with reaction with neutral oxygen (60-70%) or nitrogen (30% or less). In weakly irradiated environment atomic elements are more abundant in the neutral state. More of the ionised atoms are produced with the increase of the UV radiation what blocks these effective channels of CN destruction.

On the other hand, HCN destruction is driven by many channels in the weakest UV regime. Simultaneous impact of few different reactions is not as effective as the reaction ruling the CN destruction. It leads to higher HCN abundances compared to CN.

HCN reaction with abundant  $C^+$  is the dominant destructive reaction for slightly stronger radiation fields ( $>10^{-3}$ ). This reaction results in  $CNC^+$  production which quickly reacts with electron forming CN. That explains why CN/HCN ratio increases with larger radiation.

CN/HCN ratio is widely used as UV radiation tracer in PDRs (eg. Thi et al. 2004, Han et al. 2015). HCN photodissociates into CN molecule and H atom, while CN requires more energetic photon ( $>12.4$  eV) to be disintegrated (van Dishoeck 1987). This leads to higher abundance of CN molecules and increases CN/HCN column density ratio. Fluxes of HCN photodissociation (Fig. 11) show that this reaction has marginal contribution in nitrogen chemistry up to  $G_0 \approx 100$ .

### 5.3. Comparisons to the results from Herschel

Previous studies of energetic processes around low-mass protostars showed observational premises of the influence of UV radiation on molecules. These works focused on intermediate- $J$  CO transitions (up to 6-5) that traces gas with the kinetic temperature around 100 K. With the Water in Star-Forming Regions with the Herschel Space Observatory (WISH) project (van Dishoeck et al. 2011b) higher CO rotational transitions (up to 49-48) were studied that provided information of two temperature components seen in molecular outflows: warm with  $T_{\text{rot}} \approx 300$  K and hot with  $T_{\text{rot}} \approx 600 - 800$  K (Karska et al. 2013, Green et al. 2013). The observations of the water molecule shows a broad and medium-broad components associated with non-dissociative  $C$  shocks and dissociative  $J$  shocks respectively (Kristensen et al. 2013, Mottram et al. 2014). These spectral components can be correlated to the CO rotational temperature components (Kristensen et al. 2017). Another tracers sensitive to UV radiation, ionised hydrides such as  $CH^+$ ,  $OH^+$  and  $H_2O^+$ , were found in outflow cavities (Benz et al. 2016). The UV fluxes were estimated as  $10^2$ - $10^3$  higher than average interstellar radiation. There is no molecular evidence for influence of X-rays for chemical compositions of low-mass protostars.

Most of the low-mass protostars have a broad, centered on  $v_{\text{source}}$  CO  $J = 16 - 15$  and  $H_2O$  component in their spectra (Kristensen et al. 2017). There are typically  $\approx 20$  km s $^{-1}$  broad and associated with cavity shocks. The emitting gas is located in shocks along the outflow cavity wall or along the molecular wind alternatively (Yvart et al. 2016). Some of the sources show a narrow, offset component as well that is seen in the PACS CO ladder with  $T_{\text{rot}} \approx 600 - 800$ . The gas dissociated by UV photons and carried out from the protostar was proposed as an origin of the pre-shock gas (Kristensen et al. 2017). Thus, ultraviolet radiation can propagate in large scales of 1000 AU from the central protostar, changing the properties of the surrounding matter. The hypothesis of the UV irradiated shocks is raised also based on  $H_2O/OH$  ratio observations. The ratio showed a few order of magnitude disagreement with fully-shielded shock models (Karska et al. 2014). The observations are reproduced with predictions of  $C$ -shock models illuminated by UV photons of the strength 0.1-10 times the interstellar value (Melnick & Kaufman 2015). The other photodissociation tracers, fluxes of [OI] and [CII] are significantly higher than predicted by fully-shielded  $C$ -shock models (Karska et al. 2018). Therefore, ultraviolet radiation may play an important role in low-mass protostars surroundings.

## 6. Conclusions

IRAM 30 m / EMIR observations of CN and HCN emission pinpoint the location of the impact of UV radiation on the chemistry of low-mass star forming region in Serpens. A combination of simple models using radiative-code RADEX and chemical code Nahoon allows us to determine physical conditions of the gas, column densities of molecular species, and estimate the UV radiation field strength. The main conclusions of our study are the following.

- The spatial extent of HCN 1-0 and CN 1-0 show significant differences, with HCN resembling the CO 6-5 emission tracing outflows and CN concentrated close to the individual protostar positions or their groups.
- The ratios of CN and HCN systematically differ between protostar and outflow position, both taking into account the integrated line profile and the line wings [TBC!]. The ratio is the highest at the positions of the protostars, confirming the impact of UV identified using *Herschel* as part of the WISH program.
- For typical densities of low-mass protostellar envelopes of  $10^5$  cm $^{-3}$  and gas temperatures of 75 K (TBC), the chemical network for nitrogen-species is sensitive to UV photons. The ratio of CN and HCN is primarily driven by the UV photodissociation of HCN into CN in a broad range of UV field strength. The tracer is most useful for  $G_0 > 10^2$ .
- The column density ratios of CN and HCN equals 1-10, which corresponds to  $G_0 \approx 10^{-2}$ . These values are in agreement with, yet in the lower end of the UV field strength obtained using  $H_2O$  and OH ratios from *Herschel*.

Similar observations for a larger sample of sources is needed to fully exploit the impact of UV radiation on the physical and chemical conditions in low-mass star forming regions. Detailed 3D modelling of protostellar envelopes with outflow cavities is necessary to fully constrain the strengths of the UV fields in physical components of young stellar objects.

**Acknowledgements.** AM, AK, MG and MŻ acknowledge support from the Polish National Science Center grant 2016/21/D/ST9/01098. AK acknowledges support from the First TEAM grant of the Foundation for Polish Science No. POIR.04.04.00-00-5D21/18-00 and the hospitality of the StarPlan group in the University of Copenhagen during the manuscript preparation. Support for this work was provided by the Polish National Agency for Academic Exchange through the project InterAPS. This research has made use of data from the Herschel Gould Belt survey (HGBS) project (<http://gouldbelt-herschel.cea.fr>). The HGBS is a Herschel Key Programme jointly carried out by SPIRE Specialist Astronomy Group 3 (SAG 3), scientists of several institutes in the PACS Consortium (CEA Saclay, INAF-IFSI Rome and INAF-Arcetri, KU Leuven, MPIA Heidelberg), and scientists of the Herschel Science Center (HSC).

## References

- André, P., Men'shchikov, A., Bontemps, S., et al. 2010, *A&A*, 518, L102  
 Bachiller, R., Pérez Gutiérrez, M., Kumar, M. S. N., & Tafalla, M. 2001, *A&A*, 372, 899  
 Benz, A. O., Bruderer, S., van Dishoeck, E. F., et al. 2016, *A&A*, 590, A105  
 Bruderer, S., Benz, A. O., Doty, S. D., van Dishoeck, E. F., & Bourke, T. L. 2009, *ApJ*, 700, 872  
 Casali, M. M., Eiroa, C., & Duncan, W. D. 1993, *A&A*, 275, 195  
 Cesaroni, R. 2005, *Ap&SS*, 295, 5  
 Chapillon, E., Guilloteau, S., Dutrey, A., Piétu, V., & Guélin, M. 2012, *A&A*, 537, A60  
 Cravens, T. E. & Dalgarno, A. 1978, *ApJ*, 219, 750  
 Daniel, F., Gérin, M., Roueff, E., et al. 2013, *A&A*, 560, A3  
 Davis, C. J., Matthews, H. E., Ray, T. P., Dent, W. R. F., & Richer, J. S. 1999, *MNRAS*, 309, 141  
 de Graauw, T., Helmich, F. P., Phillips, T. G., et al. 2010, *A&A*, 518, L6

Table 6: Comparison of different line ratios

Lines	SMM1	SMM3r	SMM3c	SMM3b	SMM4b	Ref.
[OI](63 $\mu$ m) / o-H <sub>2</sub> O(179 $\mu$ m)	8.58	1.31	2.60	2.21	2.19	1, 2
OH(84 $\mu$ m) / o-H <sub>2</sub> O(179 $\mu$ m)	0.96	0.13	0.23	0.16	0.10	1, 2
[OI](63 $\mu$ m) / OH(84 $\mu$ m)	8.98	9.76	11.39	13.69	22.17	1, 2
CH <sup>+</sup> (1-0) / OH <sup>+</sup> (1-0)	0.70	-	-	-	-	3
OH <sup>+</sup> (1-0) / o-H <sub>2</sub> O <sup>+</sup> (1-0)	$\geq 15.96$	-	-	-	-	3
C <sup>+</sup> / CH <sup>+</sup> (1-0)	0.16	-	-	-	-	3
CN(1-0) / HCN(1-0)	0.61	0.79	0.85	0.86	0.46	This work

**References.** (1) Goicoechea et al. (2012); (2) Dionatos et al. (2013); (3) Benz et al. (2016).

- Di Francesco, J., Johnstone, D., Kirk, H., MacKenzie, T., & Ledwosinska, E. 2008, *ApJS*, 175, 277
- Dionatos, O., Jørgensen, J. K., Green, J. D., et al. 2013, *A&A*, 558, A88
- Dionatos, O., Nisini, B., Codella, C., & Giannini, T. 2010, *A&A*, 523, A29
- Doty, S. D. & Neufeld, D. A. 1997, *ApJ*, 489, 122
- Dunham, M. M., Allen, L. E., Evans, Neal J., I., et al. 2015, *ApJS*, 220, 11
- Enoch, M. L., Evans, Neal J., I., Sargent, A. I., & Glenn, J. 2009, *ApJ*, 692, 973
- Enoch, M. L., Glenn, J., Evans, Neal J., I., et al. 2007, *ApJ*, 666, 982
- Evans, Neal J., I., Dunham, M. M., Jørgensen, J. K., et al. 2009, *ApJS*, 181, 321
- Frank, A., Ray, T. P., Cabrit, S., et al. 2014, *Protostars and Planets VI*, University of Arizona Press (2014), eds. H. Beuther, R. Klessen, C. Dullemond, Th. Henning [arXiv:1402.3553]
- Fuente, A., Martin-Pintado, J., Cernicharo, J., & Bachiller, R. 1993, *A&A*, 276, 473
- Fuente, A., Martin-Pintado, J., & Gaume, R. 1995, *ApJ*, 442, L33
- Gerin, M., Neufeld, D. A., & Goicoechea, J. R. 2016, *ARA&A*, 54, 181
- Goicoechea, J. R., Cernicharo, J., Karska, A., et al. 2012, *A&A*, 548, A77
- Goldsmith, P. F., Snell, R. L., Hemeon-Heyer, M., & Langer, W. D. 1984, *ApJ*, 286, 599
- Green, J. D., Evans, II, N. J., Jørgensen, J. K., et al. 2013, *ApJ*, 770, 123
- Green, J. D., Yang, Y.-L., Evans, Neal J., I., et al. 2016, *AJ*, 151, 75
- Griffin, M. J., Abergel, A., Abreu, A., et al. 2010, *A&A*, 518, L3
- Güsten, R., Baryshev, A., Bell, A., et al. 2008, *Society of Photo-Optical Instrumentation Engineers (SPIE) Conference Series*, Vol. 7020, Submillimeter heterodyne arrays for APEX, 702010
- Han, X. H., Zhou, J. J., Wang, J. Z., et al. 2015, *Astronomy and Astrophysics*, 576, A131
- Harsono, D., van Dishoeck, E. F., Bruderer, S., Li, Z. Y., & Jørgensen, J. K. 2015, *A&A*, 577, A22
- Harvey, P., Merin, B., Huard, T. L., et al. 2007, *ApJ*, 663, 1149
- Heays, A. N., Bosman, A. D., & van Dishoeck, E. F. 2017, *A&A*, 602, A105
- Herczeg, G. J., Karska, A., Bruderer, S., et al. 2012, *A&A*, 540, A84
- Hurt, R. L. & Barsony, M. 1996, *ApJ*, 460, L45
- Karska, A., Herczeg, G. J., van Dishoeck, E. F., et al. 2013, *A&A*, 552, A141
- Karska, A., Kaufman, M. J., Kristensen, L. E., et al. 2018, *ApJS*, 235, 30
- Karska, A., Kristensen, L. E., van Dishoeck, E. F., et al. 2014, *A&A*, 572, A9
- Kasemann, C., Güsten, R., Heyminck, S., et al. 2006, *Society of Photo-Optical Instrumentation Engineers (SPIE) Conference Series*, Vol. 6275, CHAMP<sup>+</sup>: a powerful array receiver for APEX, 62750N
- Klein, B., Philipp, S. D., Krämer, I., et al. 2006, *A&A*, 454, L29
- Kristensen, L. E., Gustafsson, M., Field, D., et al. 2003, *A&A*, 412, 727
- Kristensen, L. E., van Dishoeck, E. F., Benz, A. O., et al. 2013, *A&A*, 557, A23
- Kristensen, L. E., van Dishoeck, E. F., Mottram, J. C., et al. 2017, *A&A*, 605, A93
- Kristensen, L. E., van Dishoeck, E. F., van Kempen, T. A., et al. 2010, *A&A*, 516, A57
- Kroupa, P. 2002, *Science*, 295, 82
- Lee, K. I., Fernández-López, M., Storm, S., et al. 2014, *ApJ*, 797, 76
- Loughnane, R. M., Redman, M. P., Thompson, M. A., et al. 2012, *MNRAS*, 420, 1367
- Melnick, G. J. & Kaufman, M. J. 2015, *ApJ*, 806, 227
- Mottram, J. C., Kristensen, L. E., van Dishoeck, E. F., et al. 2014, *A&A*, 572, A21
- Myers, P. C. & Ladd, E. F. 1993, *ApJ*, 413, L47
- Neufeld, D. A. & Dalgarno, A. 1989, *ApJ*, 344, 251
- Ortiz-León, G. N., Dzib, S. A., Koungkel, M. A., et al. 2017, *ApJ*, 834, 143
- Ossenkopf, V., Müller, H. S. P., Lis, D. C., et al. 2010, *A&A*, 518, L111
- Pickett, H. M., Poynter, R. L., Cohen, E. A., et al. 1998, *J. Quant. Spectr. Rad. Transf.*, 60, 883
- Poglitsch, A., Waelkens, C., Geis, N., et al. 2010, *A&A*, 518, L2
- Riaz, B., Thi, W. F., & Caselli, P. 2018, *MNRAS*, 481, 4662
- Schöier, F. L., van der Tak, F. F. S., van Dishoeck, E. F., & Black, J. H. 2005, *A&A*, 432, 369
- Skatrud, D. D., De Lucia, F. C., Blake, G. A., & Sastry, K. V. L. N. 1983, *Journal of Molecular Spectroscopy*, 99, 35
- Skrutskie, M. F., Cutri, R. M., Stiening, R., et al. 2006, *AJ*, 131, 1163
- Spaans, M., Hogerheijde, M. R., Mundy, L. G., & van Dishoeck, E. F. 1995, *ApJ*, 455, L167
- Stäuber, P., Benz, A. O., Jørgensen, J. K., et al. 2007, *A&A*, 466, 977
- Stäuber, P., Doty, S. D., van Dishoeck, E. F., & Benz, A. O. 2005, *A&A*, 440, 949
- Suresh, A., Dunham, M. M., Arce, H. G., et al. 2016, *AJ*, 152, 36
- Tercero, B., Cernicharo, J., Pardo, J. R., & Goicoechea, J. R. 2010, *A&A*, 517, A96
- Testi, L. & Sargent, A. I. 1998, *ApJ*, 508, L91
- Thi, W. F., van Zadelhoff, G. J., & van Dishoeck, E. F. 2004, *Astronomy and Astrophysics*, 425, 955
- van der Tak, F. F. S., Black, J. H., Schöier, F. L., Jansen, D. J., & van Dishoeck, E. F. 2007, *A&A*, 468, 627
- van Dishoeck, E. F. 1987, in *IAU Symposium*, Vol. 120, *Astrochemistry*, ed. M. S. Vardya & S. P. Tarafdar, 51–65
- van Dishoeck, E. F., Kristensen, L. E., Benz, A. O., et al. 2011a, *PASP*, 123, 138
- van Dishoeck, E. F., Kristensen, L. E., Benz, A. O., et al. 2011b, *PASP*, 123, 138
- van Kempen, T. A., van Dishoeck, E. F., Güsten, R., et al. 2009, *A&A*, 507, 1425
- Wakelam, V., Herbst, E., Loison, J. C., et al. 2012, *ApJS*, 199, 21
- Walker-Smith, S. L., Richer, J. S., Buckle, J. V., Hatchell, J., & Drabek-Maunders, E. 2014, *MNRAS*, 440, 3568
- Wampfler, S. F., Bruderer, S., Karska, A., et al. 2013, *A&A*, 552, A56
- Wright, E. L., Eisenhardt, P. R. M., Mainzer, A. K., et al. 2010, *AJ*, 140, 1868
- Wyrowski, F., Menten, K. M., Güsten, R., & Belloche, A. 2010, *A&A*, 518, A26
- Yang, Y.-L., Green, J. D., Evans, Neal J., I., et al. 2018, *ApJ*, 860, 174
- Yildiz, U. A., Kristensen, L. E., van Dishoeck, E. F., et al. 2012, *A&A*, 542, A86
- Yildiz, U. A., Kristensen, L. E., van Dishoeck, E. F., et al. 2015, *A&A*, 576, A109
- Yvart, W., Cabrit, S., Pineau des Forêts, G., & Ferreira, J. 2016, *A&A*, 585, A74
- Zinnecker, H. & Yorke, H. W. 2007, *ARA&A*, 45, 481

## Appendix A: Spectral Energy Distributions

Broad-band observations are needed in order to determine physical properties of a protostar. Dunham et al. 2015 studied properties of protostars in the Serpens molecular cloud using 2MASS (Skrutskie et al. 2006) and Spitzer IRAC/MIPS (Evans et al. 2009), observations covering the range of  $1.25\text{--}70\text{ }\mu\text{m}$ , photometry from Wide-field Infrared Survey Explorer 12 and  $22\text{ }\mu\text{m}$  (WISE; Wright et al. 2010), SHARC-II  $350\text{ }\mu\text{m}$  (Suresh et al. 2016), the SCUBA Legacy Catalog  $450$  and  $850\text{ }\mu\text{m}$  (Di Francesco et al. 2008) and  $1.1\text{ mm}$  observations from Bolocam dust survey (Enoch et al. 2007). The Serpens Main region was also observed during the Herschel Gould Belt survey project (André et al. 2010) at  $70$ ,  $160$ ,  $250$ ,  $350$  and  $500\text{ }\mu\text{m}$ . SPIRE/PACS photometry in the Serpens molecular cloud is discussed in Fiorellino et al. (in prep.). The flux densities used in the SED analysis are in Tab. A.1.

Based on SEDs the bolometric temperature and luminosity can be calculated for each of the observed protostars. The bolometric luminosity was determined by integrating the SEDs over frequency:

$$L_{bol} = \pi d^2 \int F_\nu d\nu \quad (\text{A.1})$$

where  $d$  is the cloud distance of  $436 \pm 9.2\text{ pc}$  (Ortiz-León et al. 2017). The bolometric temperature was calculating as described in Myers & Ladd 1993:

$$T_{bol} = 1.25 \cdot 10^{-11} \bar{\nu} \quad (\text{A.2})$$

where  $\bar{\nu}$  is the mean frequency given by:

$$\bar{\nu} = \frac{\int \nu F_\nu d\nu}{\int F_\nu d\nu} \quad (\text{A.3})$$

Using Scipy *splrep* and *splev* functions cubic smooth spline interpolation of the photometric data was performed while calculating the protostars parameters. Integration along the resulting axis was obtain with the composite trapezoidal rule (*Scipy* package). The photometric data allows us to perform the integration along wide range of wavelength with exception of SMM8. Here we have only 4 photometric points from the Herschel Gould Belt so the calculated bolometric luminosity and temperature can be underestimated.

## Appendix B: Maps in additional tracers

IRAM 30m spectral line maps in HCN and CS isotopologues are presented in Fig. B.1 and Fig. B.2. The  $\text{H}^{13}\text{CN } J = 1 - 0$  emission is a sum of all hyperfine splitting components. The  $\text{H}^{13}\text{CN } J = 1 - 0$  is spatially consistent with  $\text{HCN } J = 1 - 0$ , although a few times weaker. It peaks around Ser-SMM2, Ser-SMM4 and Ser-SMM9, as well as at the Outflow position no. 3. Except for the Ser-SMM2 protostar, the peaks in  $\text{H}^{13}\text{CN}$  are co-spatial with the HCN emission peaks. The emission of  $\text{H}^{13}\text{CN } J = 1 - 0$  line is similarly strong in the SE and NW regions of the map.

The  $\text{C}^{34}\text{S } J = 3 - 2$  line does not show such extended emission, although it was detected in all outflow positions. The emission is concentrated mostly near Ser-SMM1, Ser-SMM4 and Ser-SMM9 sources, unlike the  $\text{CS } J = 3 - 2$  which is not that significant around Ser-SMM1. The isotopologues trace the same gas as their regular counterparts.

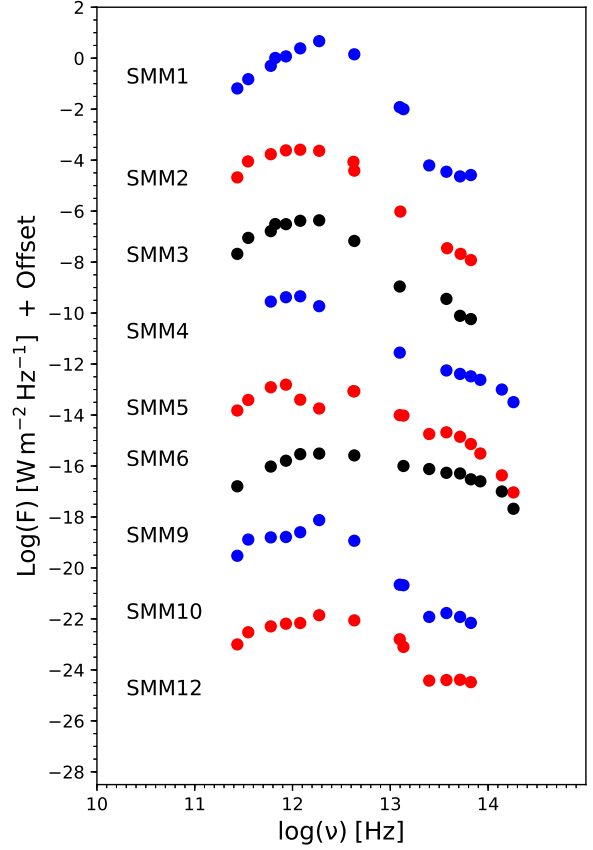


Fig. A.1: Spectral Energy Distributions of protostars in the Serpens Main region.

## Appendix C: Molecular line profiles

The targeted lines were detected in most of the protostars and outflow positions. Fig. C.1 shows the spectra in  $\text{C}^{34}\text{S } J = 3 - 2$ ,  $\text{CS } J = 3 - 2$ ,  $\text{H}^{13}\text{CN } J = 2 - 1$ ,  $\text{H}^{13}\text{CN } J = 1 - 0$ ,  $\text{HCN } J = 1 - 0$  and  $\text{CN } J = 1 - 0$  lines obtained with the IRAM 30m, as well as profiles in  $\text{CO } J = 6 - 5$  observed with APEX-CHAMP<sup>+</sup>. The spectra at the Ser-SMM4 position are shown in Fig. 3.2. The  $\text{H}^{13}\text{CN } J = 2 - 1$  line was detected only at Ser-SMM4 and Ser-SMM9 sources. The Ser-SMM8 protostar is outside of the mapping area in  $\text{CO } J = 6 - 5$ .

## Appendix D: Line fluxes and observed column densities

Table D.1 lists the observed lines and their properties calculated at protostars positions. The integrated intensity  $T_{mb} dV$  of a line is measured at  $3\sigma$  level for each spectrum separately. The peak temperature  $T_{peak}$  is the value at the maximum of a line or of the strongest hyperfine component. Column densities at the upper level  $N_{up}$  and total column densities  $N_{tot}$  were calculated as described in §4.1 (Eq. 3 and Eq. 4).

## Appendix E: RADEX models

RADEX models predictions for hydrogen densities ranged  $10^4 - 10^6\text{ cm}^{-3}$  and kinetic temperature of a gas of  $30 - 200\text{ K}$  are presented in Fig. E.1. CN and HCN column densities ratios inferred by the models comparison with observations (blue and green rectangles) are shown in Tab. 4.

Table A.1: Flux densities in Jy, corrected for the beam size.

$\lambda$ ( $\mu\text{m}$ )	SMM1	SMM2	SMM3	SMM4	SMM5	SMM6	SMM9	SMM10	SMM12
1.25	-	-	-	$6.0 \times 10^{-4}$	$3.0 \times 10^{-4}$	$2.1 \times 10^{-2}$	-	-	-
1.65	-	-	-	$3.2 \times 10^{-3}$	$9.0 \times 10^{-4}$	$2.1 \times 10^{-1}$	-	-	-
2.17	-	-	-	$1.0 \times 10^{-2}$	$4.3 \times 10^{-3}$	$1.0 \times 10^0$	-	-	-
3.6	$9.0 \times 10^{-4}$	$4.0 \times 10^{-4}$	$2.8 \times 10^{-3}$	$2.4 \times 10^{-2}$	$3.1 \times 10^{-2}$	$2.5 \times 10^0$	$2.0 \times 10^{-3}$	$7.4 \times 10^{-3}$	$2.8 \times 10^{-3}$
4.5	$2.6 \times 10^{-3}$	$1.2 \times 10^{-3}$	$5.8 \times 10^{-3}$	$3.3 \times 10^{-2}$	$7.3 \times 10^{-2}$	$3.0 \times 10^0$	$7.0 \times 10^{-3}$	$3.3 \times 10^{-2}$	$3.0 \times 10^{-2}$
5.8	$2.3 \times 10^{-3}$	$2.1 \times 10^{-3}$	$7.8 \times 10^{-3}$	$4.1 \times 10^{-2}$	$1.4 \times 10^{-1}$	$5.1 \times 10^0$	$1.2 \times 10^{-2}$	$4.1 \times 10^{-2}$	$1.0 \times 10^{-1}$
8.0	$3.5 \times 10^{-3}$	$3.5 \times 10^{-3}$	$3.6 \times 10^{-2}$	$5.6 \times 10^{-2}$	$2.1 \times 10^{-1}$	$5.4 \times 10^0$	$1.7 \times 10^{-2}$	-	$2.0 \times 10^{-1}$
12.0	$6.2 \times 10^{-3}$	-	-	-	$1.8 \times 10^{-1}$	$7.6 \times 10^0$	$1.2 \times 10^{-2}$	$3.8 \times 10^{-2}$	$2.2 \times 10^{-1}$
22.0	$1.0 \times 10^0$	-	-	-	$9.5 \times 10^{-1}$	$1.0 \times 10^1$	$2.1 \times 10^{-1}$	$8.0 \times 10^{-1}$	$3.1 \times 10^0$
24.0	$1.2 \times 10^0$	$1.0 \times 10^{-1}$	$1.1 \times 10^{-1}$	$2.8 \times 10^{-1}$	$9.9 \times 10^{-1}$	-	$2.2 \times 10^{-1}$	$1.6 \times 10^0$	$2.6 \times 10^0$
70.0	$1.4 \times 10^2$	$3.9 \times 10^0$	$6.8 \times 10^0$	-	$8.5 \times 10^0$	$2.6 \times 10^1$	$1.2 \times 10^1$	$8.8 \times 10^0$	$3.3 \times 10^0$
160.0	$4.7 \times 10^2$	$2.3 \times 10^1$	$4.4 \times 10^1$	$1.9 \times 10^1$	$1.8 \times 10^0$	$3.1 \times 10^1$	$7.5 \times 10^1$	$1.4 \times 10^1$	$2.0 \times 10^1$
250.0	$2.4 \times 10^2$	$2.6 \times 10^1$	$4.2 \times 10^1$	$4.6 \times 10^1$	$4.0 \times 10^0$	$2.9 \times 10^1$	$2.5 \times 10^1$	$6.9 \times 10^0$	$3.2 \times 10^1$
350	$1.2 \times 10^2$	$2.4 \times 10^1$	$3.1 \times 10^1$	$4.2 \times 10^1$	$1.6 \times 10^1$	$1.6 \times 10^1$	$1.6 \times 10^1$	$6.5 \times 10^0$	$3.1 \times 10^1$
450.0	$1.0 \times 10^2$	-	$3.1 \times 10^1$	-	-	-	-	-	-
500	$5.0 \times 10^1$	$1.7 \times 10^1$	$1.6 \times 10^1$	$2.8 \times 10^1$	$1.2 \times 10^1$	$9.5 \times 10^0$	$1.6 \times 10^1$	$5.1 \times 10^0$	$1.6 \times 10^1$
850.0	$1.5 \times 10^1$	$8.9 \times 10^0$	$8.9 \times 10^0$	-	$3.9 \times 10^0$	-	$1.3 \times 10^1$	$3.0 \times 10^0$	-
1100.0	$6.5 \times 10^0$	$2.1 \times 10^0$	$2.1 \times 10^0$	-	$1.5 \times 10^0$	$1.6 \times 10^0$	$3.0 \times 10^0$	$1.0 \times 10^0$	$2.1 \times 10^0$

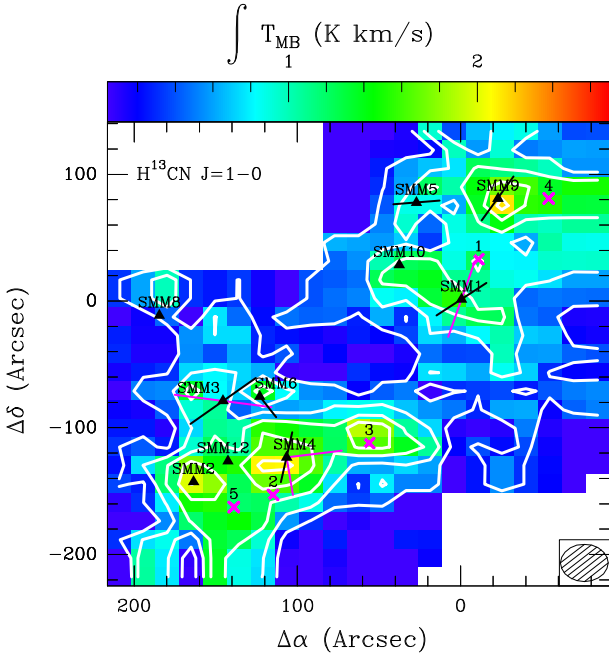


Fig. B.1: Similar to Fig. 2 but the emission of the  $\text{H}^{13}\text{CN } J = 1 - 0$  line. The first contour at  $10 \sigma$  level, with step of  $10 \sigma$

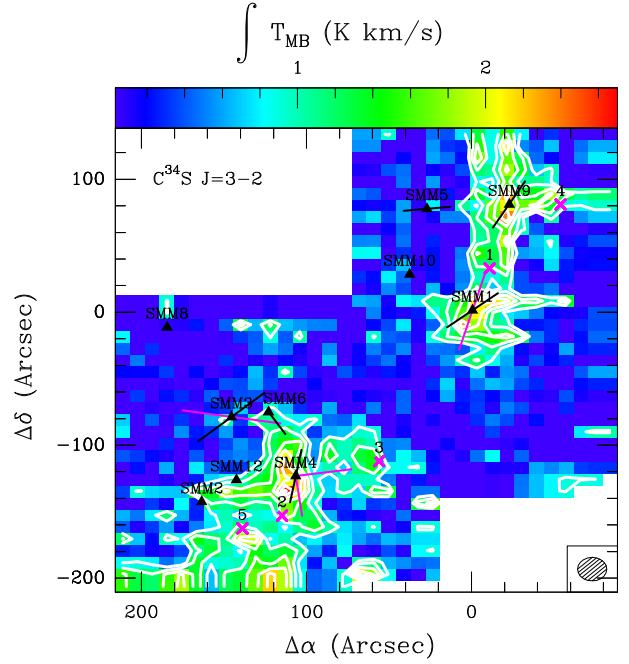


Fig. B.2: Similar to Fig. 2 but the emission of the  $\text{C}^{34}\text{S } J = 3 - 2$  line. The first contour at  $30 \sigma$  level, with step of  $10 \sigma$

## Appendix F: Dominant reactions in CN, HCN chemistry

Dominant processes in CN and HCN reactions modelled at the temperature of 50 K are listed in Tab. 5. The processes are illustrated in the Nahoon model parameter space: main channels of HCN and CN destruction, as well as HCN and CN production (Fig. 11 and Fig. F.1 - Fig. F.3 respectively). Only the reactions contributing at least 30% in total flux were taken into consideration. Dominant reactions are more dependent on the strength of the UV radiation than on the hydrogen density. Reaction networks for UV radiation in

weak ( $G_0 = 10^{-4} - 10^{-1}$ ), intermediate ( $G_0 = 10^{-1} - 10^1$ ) and strong ( $G_0 = 10^1 - 10^6$ ) regime are presented in Fig. F.4, Fig. 10 and Fig. F.5 respectively. Not only the dominant reactions, but also the main route of the reactants production were illustrated. The dominant processes modelled assuming the temperature of 200 K are listed in Tab. F.1.

## Appendix G: Correlations with $T_{\text{bol}}$ and $L_{\text{bol}}$

Fig. G.1 compares the luminosity in CN 1-0, HCN 1-0 and CS 3-2 lines in respect to the bolometric luminosities and temperatures of the observed protostars. A molecule luminosity



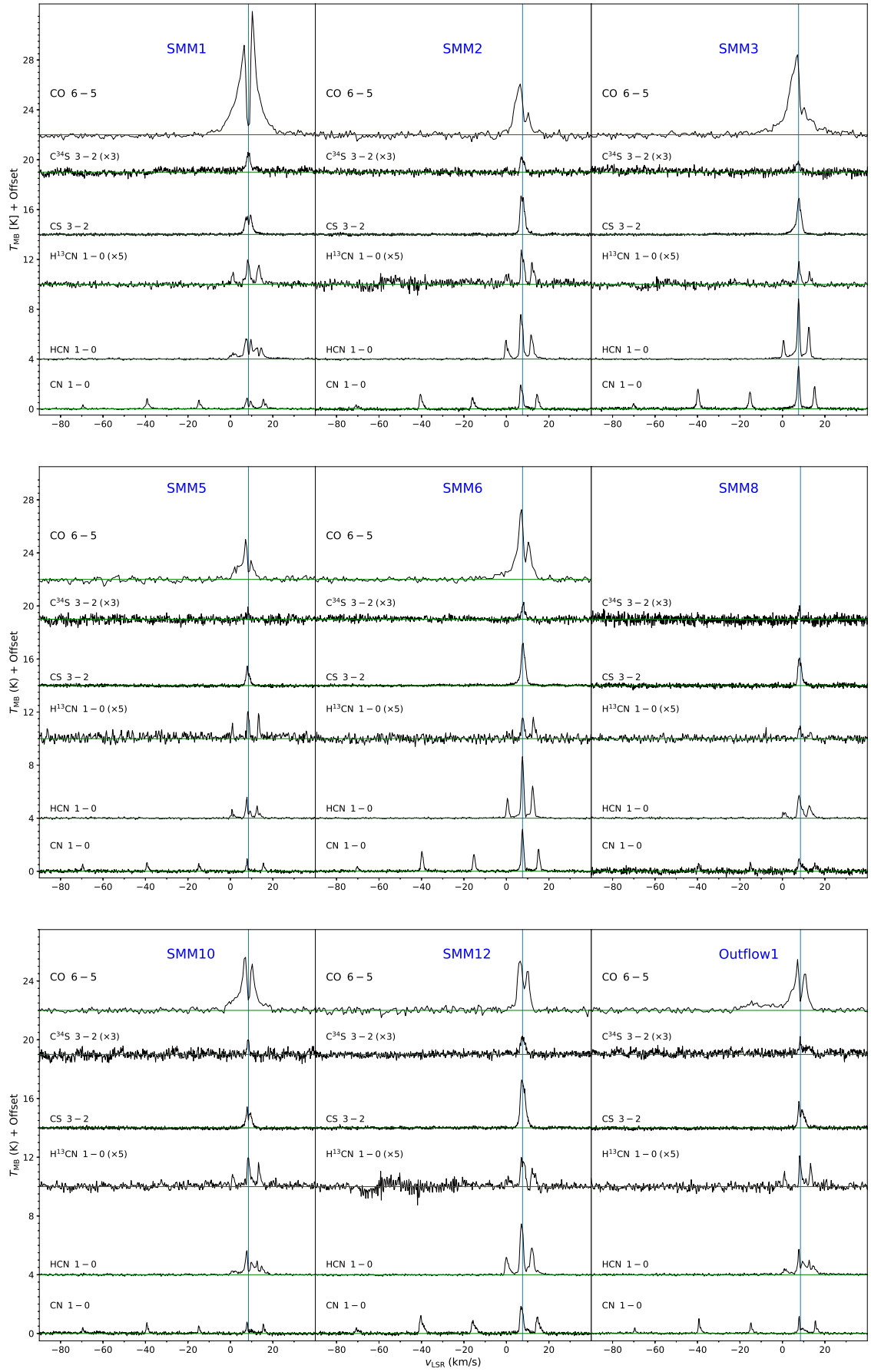


Table D.1: Integrated fluxes of the observed line at the positions of protostars

Line		SMM1	SMM2	SMM3	SMM4	SMM5	SMM6	SMM8	SMM9	SMM10	SMM12
CN 1-0	$\int T_{\text{mb}} dV$ (K km/s)	6.29	8.52	12.16	10.22	2.72	10.62	2.97	4.90	2.96	10.06
	$T_{\text{peak}}$ (K)	0.89	1.92	3.42	1.90	0.94	3.17	0.94	0.84	0.78	1.85
	$N_{\text{up}}$ (cm <sup>-2</sup> )	$1.3 \times 10^{13}$	$1.8 \times 10^{13}$	$2.6 \times 10^{13}$	$2.2 \times 10^{13}$	$5.7 \times 10^{12}$	$2.2 \times 10^{13}$	$6.2 \times 10^{12}$	$1.0 \times 10^{13}$	$6.2 \times 10^{12}$	$2.1 \times 10^{13}$
	$N_{\text{tot}}$ (cm <sup>-2</sup> )	$7.9 \times 10^{14}$	$1.1 \times 10^{15}$	$1.5 \times 10^{15}$	$1.3 \times 10^{15}$	$3.4 \times 10^{14}$	$1.3 \times 10^{15}$	$3.7 \times 10^{14}$	$6.2 \times 10^{14}$	$3.7 \times 10^{14}$	$1.3 \times 10^{15}$
HCN 1-0	$\int T_{\text{mb}} dV$ (K km/s)	10.34	13.08	14.36	21.67	4.04	13.10	6.84	20.68	7.26	14.24
	$T_{\text{peak}}$ (K)	1.76	3.48	4.95	4.69	1.72	5.15	1.72	2.40	1.75	3.50
	$N_{\text{up}}$ (cm <sup>-2</sup> )	$6.5 \times 10^{12}$	$8.3 \times 10^{12}$	$9.1 \times 10^{12}$	$1.4 \times 10^{13}$	$2.6 \times 10^{12}$	$8.3 \times 10^{12}$	$4.3 \times 10^{12}$	$1.3 \times 10^{13}$	$4.6 \times 10^{12}$	$9.0 \times 10^{12}$
	$N_{\text{tot}}$ (cm <sup>-2</sup> )	$2.5 \times 10^{14}$	$3.1 \times 10^{14}$	$3.4 \times 10^{14}$	$5.2 \times 10^{14}$	$9.6 \times 10^{13}$	$3.1 \times 10^{14}$	$1.6 \times 10^{14}$	$4.9 \times 10^{14}$	$1.7 \times 10^{14}$	$3.4 \times 10^{14}$
CS 3-2	$\int T_{\text{mb}} dV$ (K km/s)	5.89	8.56	8.30	14.76	2.56	8.50	4.51	12.43	3.58	9.88
	$T_{\text{peak}}$ (K)	1.57	3.10	2.90	4.30	1.48	3.2	2.08	2.70	1.43	3.26
	$N_{\text{up}}$ (cm <sup>-2</sup> )	$4.1 \times 10^{12}$	$5.9 \times 10^{12}$	$5.7 \times 10^{12}$	$1.0 \times 10^{13}$	$1.8 \times 10^{12}$	$5.7 \times 10^{12}$	$3.1 \times 10^{12}$	$8.6 \times 10^{12}$	$2.5 \times 10^{12}$	$6.8 \times 10^{12}$
	$N_{\text{tot}}$ (cm <sup>-2</sup> )	$4.5 \times 10^{13}$	$6.5 \times 10^{13}$	$6.3 \times 10^{13}$	$1.1 \times 10^{14}$	$2.0 \times 10^{13}$	$6.5 \times 10^{13}$	$3.4 \times 10^{13}$	$9.5 \times 10^{13}$	$2.7 \times 10^{13}$	$7.5 \times 10^{13}$
C <sup>34</sup> S 3-2	$\int T_{\text{mb}} dV$ (K km/s)	1.27	0.86	0.50	1.49	0.32	0.76	0.26	1.83	0.39	0.56
	$T_{\text{peak}}$ (K)	0.56	0.47	0.36	0.64	0.42	0.56	0.35	0.62	0.40	0.42
	$N_{\text{up}}$ (cm <sup>-2</sup> )	$7.1 \times 10^{11}$	$4.8 \times 10^{11}$	$2.8 \times 10^{11}$	$8.4 \times 10^{11}$	$1.8 \times 10^{11}$	$4.3 \times 10^{11}$	$1.4 \times 10^{11}$	$1.0 \times 10^{12}$	$2.2 \times 10^{11}$	$3.1 \times 10^{11}$
	$N_{\text{tot}}$ (cm <sup>-2</sup> )	$7.9 \times 10^{12}$	$5.4 \times 10^{12}$	$3.1 \times 10^{12}$	$9.4 \times 10^{12}$	$2.0 \times 10^{12}$	$4.8 \times 10^{12}$	$1.6 \times 10^{12}$	$1.2 \times 10^{13}$	$2.5 \times 10^{12}$	$3.5 \times 10^{12}$
H <sup>13</sup> CN 1-0	$\int T_{\text{mb}} dV$ (K km/s)	1.59	1.50	0.55	1.61	0.77	0.87	0.14	2.37	1.04	1.61
	$T_{\text{peak}}$ (K)	0.45	0.64	0.41	0.61	0.42	0.40	0.21	0.38	0.45	0.46
	$N_{\text{up}}$ (cm <sup>-2</sup> )	$3.3 \times 10^{11}$	$3.1 \times 10^{11}$	$1.6 \times 10^{11}$	$3.4 \times 10^{11}$	$1.6 \times 10^{11}$	$1.8 \times 10^{11}$	$2.9 \times 10^{10}$	$5.0 \times 10^{11}$	$2.2 \times 10^{11}$	$3.4 \times 10^{11}$
	$N_{\text{tot}}$ (cm <sup>-2</sup> )	$1.3 \times 10^{13}$	$1.2 \times 10^{13}$	$4.5 \times 10^{12}$	$1.3 \times 10^{13}$	$6.2 \times 10^{12}$	$7.0 \times 10^{12}$	$1.1 \times 10^{12}$	$1.9 \times 10^{13}$	$8.4 \times 10^{12}$	$1.3 \times 10^{13}$

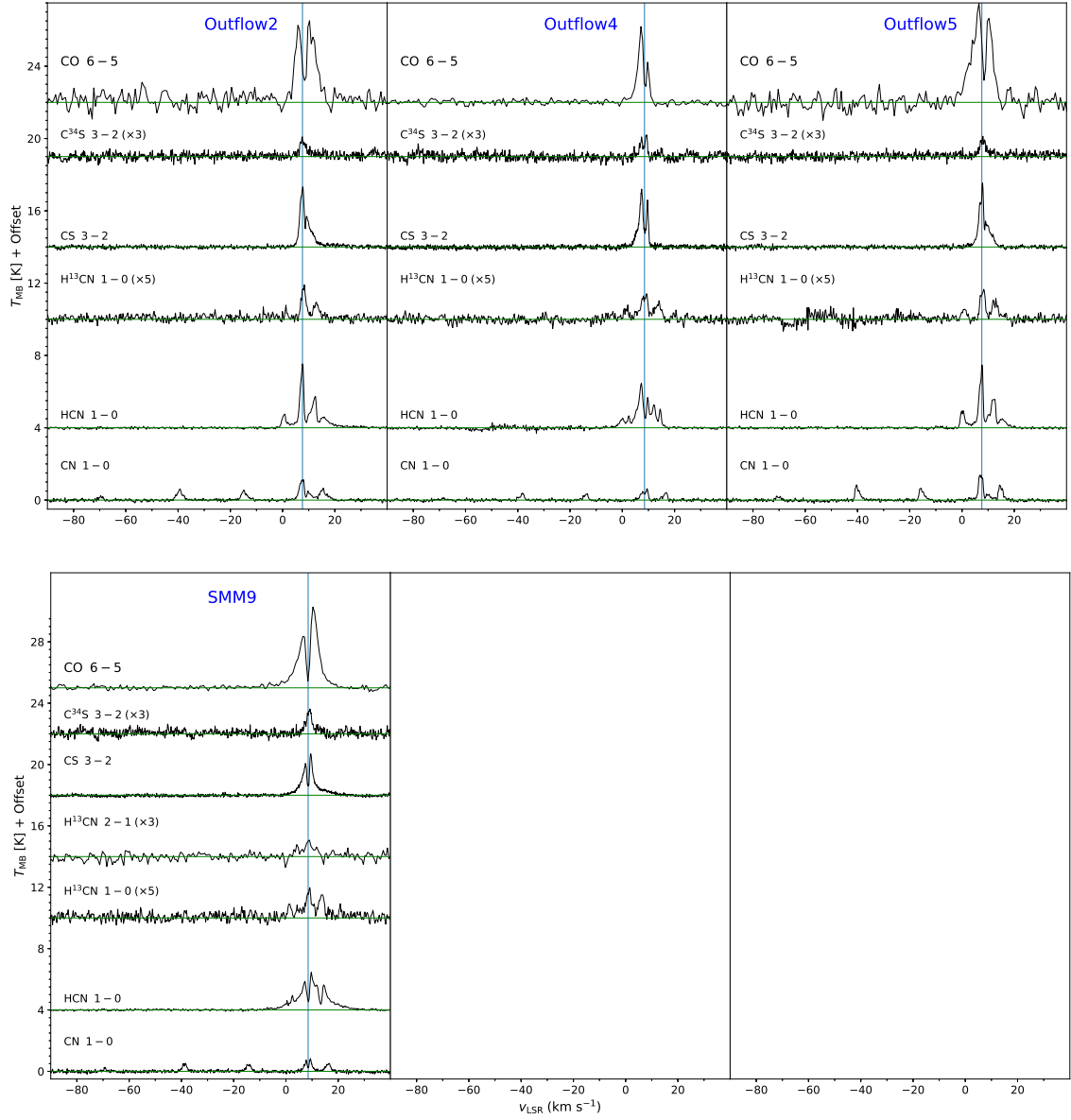


Fig. C.1: Serpens Main sources spectra of CO(6-5),  $C^{34}S(3-2)$ , CS(3-2),  $H^{13}CN(2-1)$ ,  $H^{13}CN(1-0)$ , HCN(1-0) and CN(1-0) lines.

is calculated based on the integrated intensity of a line at  $3\sigma$  level. The integrated flux in  $K km s^{-1}$  unit is converted to  $Jy km s^{-1}$  using conversion factors  $Jy/K$  tabularised in 'Proposals for IRAM Telescopes' document<sup>3</sup>. Then,  $Jy$  is converted to  $W$  and divided by the wavelength in  $km$ . The luminosity in a line is calculated by the standard relation between luminosity  $L$  and flux  $F$  (Eq. G.1) and expressed in solar luminosities.

$$L = F 4 \pi d^2 \quad (G.1)$$

where distance  $d$  is  $436 \pm 9.2 pc$  (Ortiz-León et al. 2017).

<sup>3</sup> www.iram.fr

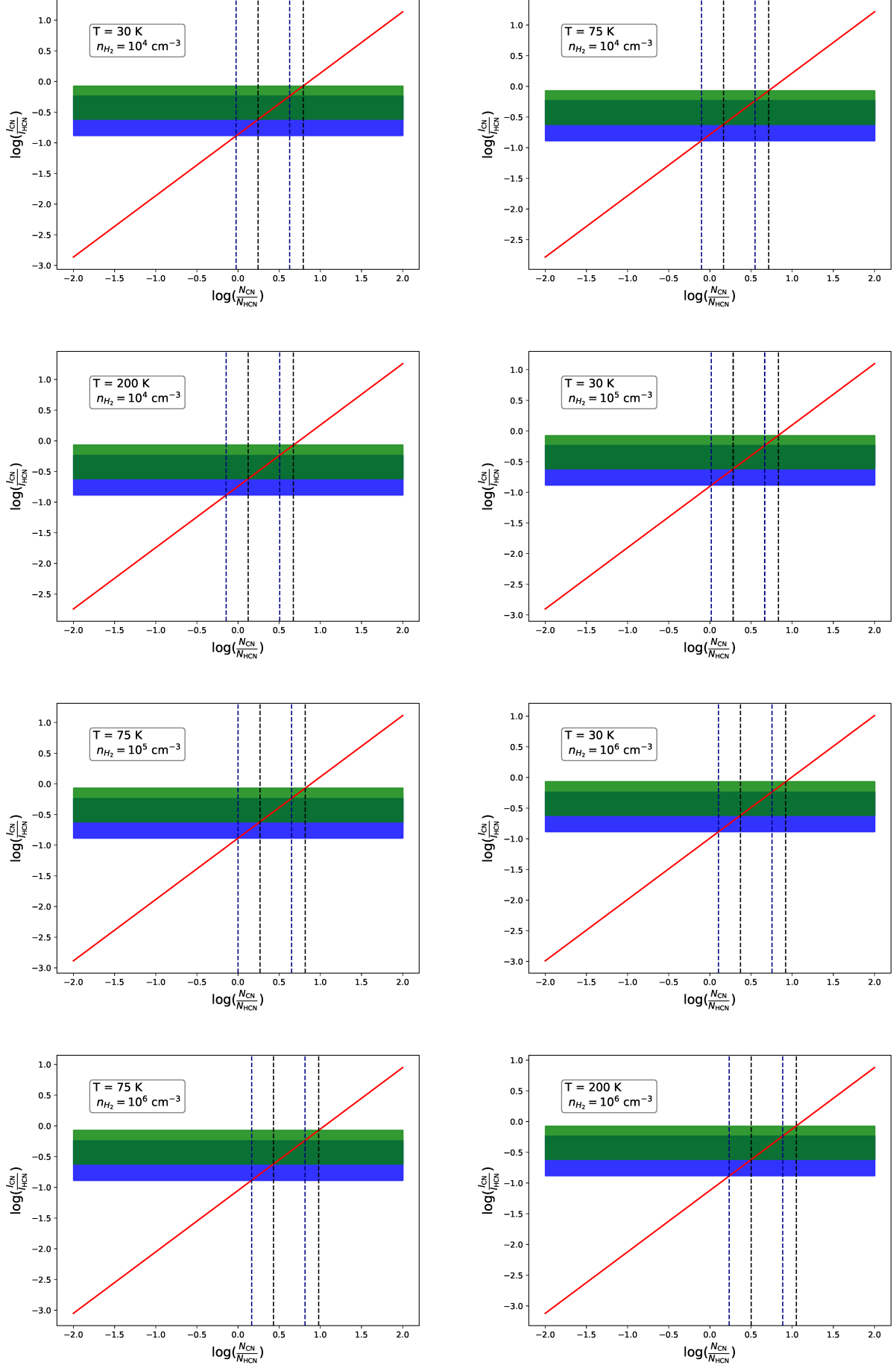


Table F.1: Dominant processes in CN, HCN chemistry - outflow (200K)

Molecule	Weak UV fields ( $G_0 = 10^{-4} - 10^{-1}$ )	Medium UV fields ( $G_0 = 10^{-1} - 10^1$ )	Strong UV fields ( $G_0 = 10^1 - 10^6$ )
CN	$O + CN \rightarrow N + CO$ $CN + N \rightarrow C + N_2$	<b>Destruction</b> $CN + ph \rightarrow C + N$ $O + CN \rightarrow N + CO$	$CN + ph \rightarrow C + N$
	<b>Production</b> $CNC^+ + e^- \rightarrow C + CN$ $N + C_2 \rightarrow C + CN$ $HCN + ph \rightarrow H + CN$	<b>Production</b> $N + C_2 \rightarrow C + CN$ $H + CN^+ \rightarrow CN + H^+$	$H + CN^+ \rightarrow CN + H^+$ $HCN^+ + e^- \rightarrow H + CN$ $N + C_2 \rightarrow C + CN$ $N + CH \rightarrow H + CN$ $HCN + ph \rightarrow H + CN$
		<b>Destruction</b> $HCN + C^+ \rightarrow H + CNC^+$ $HCN + ph \rightarrow H + CN$ $HCN + HCO^+ \rightarrow CO + HCNH^+$	$HCN + ph \rightarrow H + CN$ $HCN + C^+ \rightarrow H + CNC^+$
HCN	$N + CH_2 \rightarrow H + HCN$ $H + CCN \rightarrow C + HCN$ $CN + H_2 \rightarrow H + HCN$ $C + HNC \rightarrow C + HCN$	<b>Production</b> $H + CCN \rightarrow C + HCN$ $HCNH^+ + e^- \rightarrow H + HCN$	$HCNH^+ + e^- \rightarrow H + HCN$ $H + CCN \rightarrow C + HCN$ $H_2NC^+ + e^- \rightarrow H + HCN$ $N + CH_2 \rightarrow H + HCN$

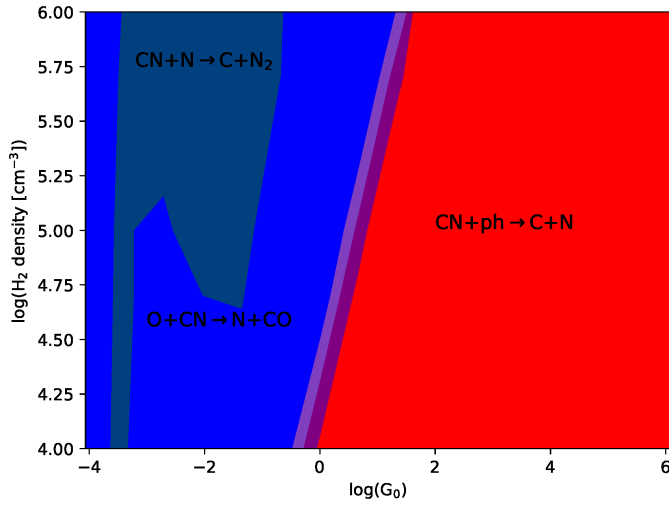


Fig. F.1: Dominant reactions of CN destruction. Reactions contributed at least 50% of total flux are marked with full colour. Transparent colours correspond to 30%-50% contribution.

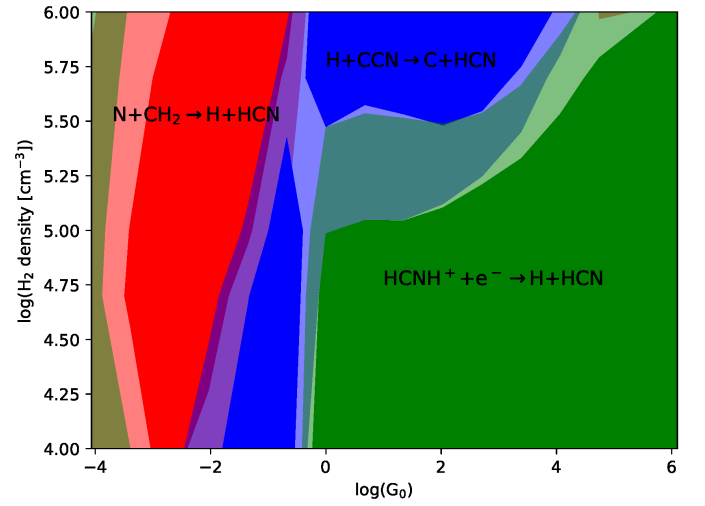


Fig. F.2: Similar to Fig. F.1 but for HCN production.

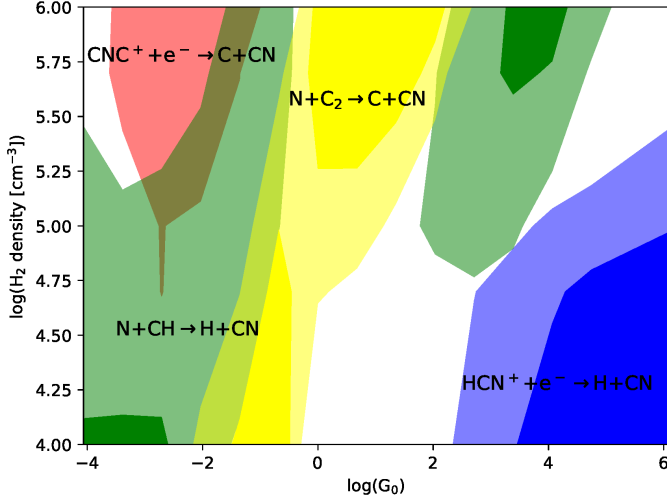


Fig. F.3: Similar to Fig. F.1 but for CN production.

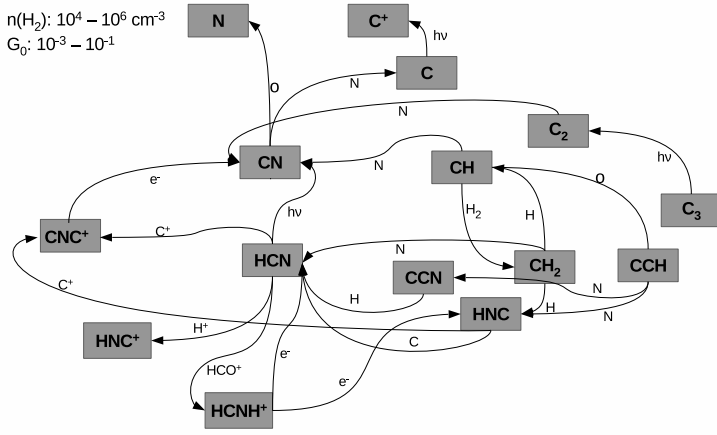


Fig. F.4: Reactions network for weakly UV irradiated gas.

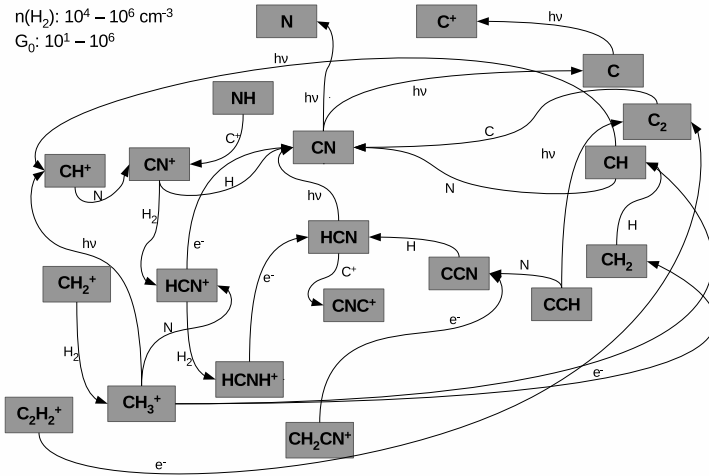


Fig. F.5: Similar to Fig. F.4 but for UV field higher than  $G_0 = 10^1$ .



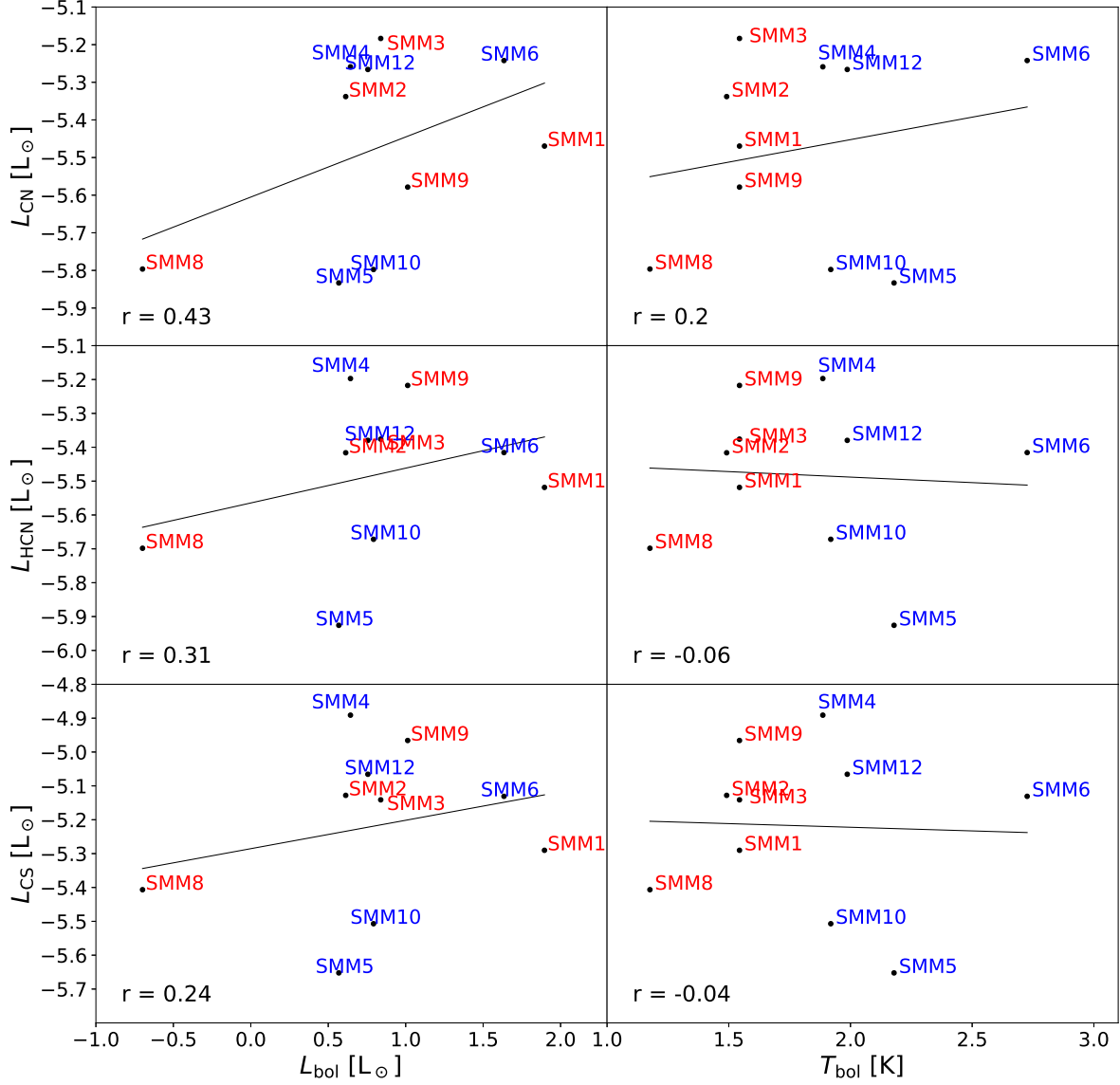


Fig. G.1: Correlations of lines luminosity with bolometric luminosity and temperature of protostars. Class 0 protostars are marked with red, while Class I with blue colour. The Pearson coefficient of the correlation ( $r$ ) is shown.